Non-monotonic relations of galaxy star formation, radius, and structure at fixed stellar mass

Jimena Stephenson,[1]★ Aldo Rodríguez-Puebla ®,[2]★ S. M. Faber,[3] Joel R. Primack,[4]
Vladimir Avila-Reese ®,[2] A. R. Calette ®,[5] Carlo Cannarozzo ®,[2,6,7] James Kakos ®,[4]
Mariana Cano-Díaz ®,[8] David C. Koo,[3] Francesco Shankar ®[9] and D. F. Morell ®[2]

[1]*University of Arizona, Tucson, Arizona 85721, USA*
[2]*Universidad Nacional Autónoma de México, Instituto de Astronomía, A. P. 70-264, 04510, Ciudad de México, México*
[3]*UCO/Lick Observatory, Department of Astronomy and Astrophysics, University of California, Santa Cruz, CA 95095, USA*
[4]*Department of Physics, University of California, Santa Cruz, CA 95064, USA*
[5]*Center for Astronomy and Astrophysics, Shanghai Jiao Tong University, Shanghai 200240, China*
[6]*New York University Abu Dhabi, PO Box 129188, Abu Dhabi, United Arab Emirates*
[7]*Center for Astrophysics and Space Science (CASS), New York University Abu Dhabi, Abu Dhabi, PO Box 129188, Abu Dhabi, United Arab Emirates*
[8]*CONACYT Research Fellow – Universidad Nacional Autónoma de México, Instituto de Astronomía, A.P. 70-264, 04510, Ciudad de México, México*
[9]*Department of Physics and Astronomy, University of Southampton, High Field SO17 1BJ, UK*

ABSTRACT

We investigate the relation between galaxy structure and star formation rate (SFR) in a sample of $\sim 2.9 \times 10^4$ central galaxies with $z < 0.0674$ and axial ratios $b/a > 0.5$. The star-forming main sequence (SFMS) shows a bend around the stellar mass of $M_* \leq M_c = 2 \times 10^{10}M_\odot$. At $M_* \leq M_c$, the SFMS follows a power-law SFR $\propto M_*^{0.85}$, while at higher masses it flattens. M_c corresponds to a dark matter halo mass of $M_{vir} \sim 10^{11.8}M_\odot$ where virial shocks occurs. Some galaxy structure (e.g. half-light radius, R_e) exhibits a non-monotonic dependence across the SFMS at a fixed M_*. We find SFR $\propto R_e^{-0.28}$ at fixed M_*, consistent with the global Kennicutt–Schmidt (KS) law. This finding suggests that galaxy sizes contribute to the scatter of the SFMS. However, at $M_* > M_c$ the relationship between SFR and R_e diminishes. Low-mass galaxies above the mean of the SFMS have smaller radii, exhibit compact and centrally concentrated profiles resembling green valley (GV) and quiescent galaxies at the same mass, and have higher M_{H_2}/M_{HI}. Conversely, those below the SFMS exhibit larger radii, lower densities, have no GV or quiescent counterparts at their mass and have lower M_{H_2}/M_{HI}. The above data suggest two pathways for quenching low-mass galaxies, $M_* \leq M_c$: a fast one that changes the morphology on the SFMS and a slow one that does not. Above M_c, galaxies below the SFMS resemble GV and quiescent galaxies structurally, implying that they undergo a structural transformation already within the SFMS. For these massive galaxies, CG are strongly bimodal, with SFMS galaxies exhibiting negative colour gradients, suggesting most star formation occurs in their outskirts, maintaining them within the SFMS.

Key words: galaxies: evolution – galaxies: star formation – galaxies: structure.

1 INTRODUCTION

Most star-forming galaxies are found to have a tight relationship between the rate at which stars are forming (star formation rate, SFR) and the total stellar mass, M_*. This relationship is called the star-forming main sequence (SFMS), and it has been observed at redshifts out to $z \sim 3$ (Daddi et al. 2007; Elbaz et al. 2007; Noeske et al. 2007; Elbaz et al. 2011; Whitaker et al. 2012; Speagle et al. 2014; Whitaker et al. 2014; Leja et al. 2022). Although the SFMS relationship evolves in time, mainly in its normalization, it maintains its tightness (Speagle et al. 2014) and high number density (Ilbert et al. 2013; Muzzin et al. 2013). This suggests that galaxies spend a significant fraction of their star-forming lifetimes within it, just like

main-sequence stars in the Hertzsprung–Russell diagram. The galaxy SFMS has become a primary tool for understanding the processes that govern the formation and evolution of galaxies as it provides insights into the mechanisms that regulate star formation within galaxies and the factors that influence the growth of galaxies over cosmic time. On the other hand, an important fraction of galaxies deviate downwards from the SFMS in a more sparse region of low values of SFRs for their masses. This quiescent galaxy fraction increases at higher masses and low redshifts, implying mass-dependent changes in their evolutionary stages. What physical mechanism(s) define the position of a galaxy *around* the SFMS or whether is *in* or *out* of it? The details about this are uncertain, but previous research has shown that it is likely related to structural changes of the galaxies and their ability to replenish their gas to keep the galaxy within the SFMS (see e.g. Schawinski et al. 2014; Tacchella et al. 2016).

Another significant parameter proposed to play an essential role in understanding galaxy evolution is the half-light radius, R_e, of the galaxy (e.g. Kauffmann et al. 2003; Omand, Balogh & Poggianti 2014; van Dokkum et al. 2015; Chen et al. 2020; Lin et al. 2020). For instance, Kauffmann et al. (2003) showed that the effective surface mass density, which combines mass and half-light radius, $\Sigma_{\rm eff} = M_*/R_e^2$, is larger for quiescent than for SF galaxies and that $\Sigma_{\rm eff} = $ const. separates SF from quiescent galaxies (see also Krajnović, Cappellari & McDermid 2018). More fundamentally, previous studies have found that SFMS galaxies are, on average, larger than quiescent galaxies for a given M_* not only locally (Shen et al. 2003) but up to higher redshifts $z \lesssim 2.5$ (van der Wel et al. 2014; Barro et al. 2017).

Galaxy sizes may be correlated with the way they quenched. van Dokkum et al. (2015) envisioned a star formation quenching model by postulating the 'parallel track' hypothesis to explain the difference of SFMS and quiescent galaxies in the size–mass plane (see also van der Wel et al. 2009; Cappellari 2016; Lilly & Carollo 2016). In this model, the *population* of galaxies follows parallel tracks in the size–mass plane, with a of slope $\Delta \log R_e/\Delta \log M_* \sim 0.3$, and they form stars at a rate dictated by the SFMS. They experience an increase in size proportional to an increase in mass and quench their SF once they cross a velocity dispersion, σ_e, threshold. This model has the profound implication that galaxies that start out with large radii will remain large in a way that R_e and SFR are nearly independent of each other. Rodríguez-Puebla et al. (2017) arrived at the conclusion that the track hypothesis was consistent with the stellar mass growth history of galaxies based on semi-empirical modelling of the galaxy–halo connection (see e.g. Wechsler & Tinker 2018; Behroozi et al. 2019) and the evolution of the size–mass relation from van der Wel et al. (2014).

Chen et al. (2020) used the parallel track hypothesis arguing that the radius of SF galaxies is the next significant parameter after mass in shaping their central supermassive black hole (SMBH) masses: for a given M_*, large galaxies host lower mass SMBHs due to their lower central 1 kpc surface densities Σ_1. Moreover, they showed that assuming SFRs to be independent of R_e on the SFMS gives the observed sloped quenching boundaries in the size–mass plane, $\Sigma_1 - M_*$, and BH–stellar mass relations, simply because larger galaxies will reach a larger stellar mass before quenching. This is consistent with van den Bosch (2016) who noted that the half-light radius, stellar masses and SMBH masses form a fundamental plane, $M_{\rm BH} \propto (M_*/R_e)^{2.9}$.

However, there are still many unknowns. Particularly, the exact shape of the relation between R_e and SFR for a given M_* is still a subject of active research, but it is generally accepted that they are weakly or almost not related, consistent with the track hypothesis. For example, Omand et al. (2014) analysed SDSS galaxies by SFR in the $R_e - M_*$ plane and found that galaxies with low SFR show smaller radii but found no significant correlation between the SFRs of SFMS galaxies and radius in normal to high-mass galaxies (see also Brennan et al. 2017; Whitaker et al. 2017; Fang et al. 2018; Lin et al. 2020, for similar results to higher z). Nevertheless, for lower-mass galaxies with $M \sim 10^{9.5} {\rm M}_\odot$, the authors noted a non-trivial dependence of SFRs, at a fixed stellar mass, on R_e. In contrast, Wuyts et al. (2011) found a strong negative correlation between SFR and R_e for highly star forming nearby galaxies: star-forming galaxies above the SFMS are a factor of ~ 2 smaller in the SDSS, with no similar trend at high redshifts.

Previous research has shown that other structural parameters, besides R_e, correlate to some degree with the SFRs when analysing both star forming and quiescent galaxies at the same stellar mass.

Quiescent galaxies tend to have higher bulge mass (Bluck et al. 2014), effective surface brightness (Kauffmann et al. 2003, 2012), Sérsic index (Bell 2008; Wuyts et al. 2011; Bell et al. 2012), and surface density within 1 kpc (Cheung et al. 2012; Fang et al. 2013; Woo & Ellison 2019; Luo et al. 2020), and tend to be of earlier morphological types (e.g. Schawinski et al. 2014).

Which structural parameter has the most influence on star formation remains unclear (but see Yesuf, Ho & Faber 2021, and below). Note, however, that some of these structural properties are in some ways mirror quantities of R_e simply because, for a given mass, quiescent galaxies are smaller (more compact) than star-forming galaxies. For example, Chen et al. (2020) showed that for a given mass, R_e maps into Σ_1 and, at the same time, Σ_1 into σ_e (see also Fang et al. 2013; Yesuf et al. 2021). If there is only a weak correlation with R_e, then it is logical to expect that these structural properties are weakly correlated as well.

Yesuf et al. (2021) used the statistical method of mutual information to quantify the relevance of several galaxy structural properties for predicting the sSFRs to a sample of face-on galaxies from the Sloan Digital Sky Survey (SDSS) Stripe 82 deep i band. These authors found that galaxies are a multiparameter family, and that morphological asymmetries (irregular spiral arms, lopsidedness, and perturbations due to mergers) are the best predictors of sSFR $\equiv$ SFR/M_* followed by bulge/concentration. SFMS galaxies with higher sSFR are more asymmetric and have stronger bulges. Nevertheless, it is unclear whether there are some variations with mass because the authors did not perform their analysis for different mass bins but for all SFMS galaxies.

The Kennicutt–Schmidt (KS) law is another fundamental relation that involves the SFR and structural parameters via the relationship between the total surface density of gas ($\Sigma_{\rm gas} = \Sigma_{\rm H{\scriptstyle I}} + \Sigma_{\rm H_2}$) and the SFR surface density (Schmidt 1959; Kennicutt 1998b; Kennicutt & Evans 2012; de los Reyes & Kennicutt 2019; Kennicutt & De Los Reyes 2021). One of the quantities directly related to the global KS law is the radius of the galaxy, which naively can be thought as the surface area $A \propto R_e^2$ (e.g. Lin et al. 2020, but see Peeples & Shankar 2011 who used the 90th percentile z-band isophotal radius, $R_{90,z}$). If the gas mass is constant for a given M_*,[1] a careful look at the global KS law quickly reveals that more compact and higher density galaxies are more star forming (SFR $\propto 1/R_e^{2(n-1)}$, where $n = 1.42$ is the exponent of the KS law). In other words, if the gas mass of SF galaxies is the same for a given M_*, a negative *monotonic relation* is expected between size and SFR from the global KS law. The above was first envisioned by Lin et al. (2020), who looked at the residuals between R_e and SFRs on both the SDSS and CANDELS/3D-HST, but found a correlation that was weaker than expected for constant gas content. The authors concluded that the gas fraction in small-radius galaxies must be smaller than the gas fraction in large radius galaxies at fixed mass.

Motivated by the results discussed above and the existence of a global KS law, our goal is to revise previous results and perform our own analysis on the relationship between SFR and the structural parameters (which can be considered as proxies for morphologies) in the local Universe, $z \sim 0.03$. Thus, this paper studies the SFR and structural parameters such as half-light radius, R_e, half-mass radius, $R_{e,*}$, central mass density within 1 kpc, Σ_1, radial colour gradient (CG), $\nabla_{(g-i)}$, and Sérsic index in the r band, n_r, in order to get a coherent picture of the dependence of the SFR on galaxy

---

[1] By fixing M_* we eliminate any correlation between mass and the size–SFR relationship.
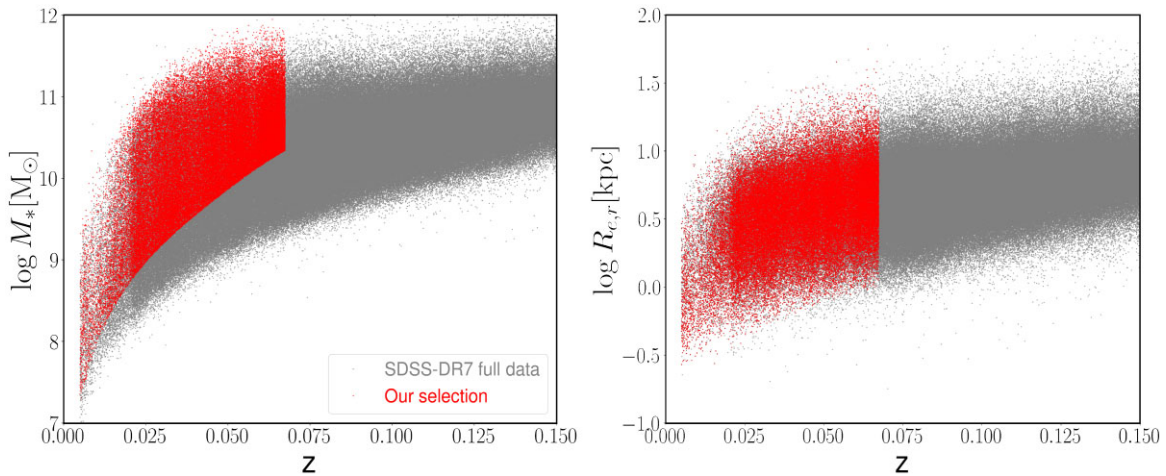
Figure 1. Stellar mass as a function of redshift and *r*-band effective radius as a function of redshift, shown in left and right panels, respectively. Our fiducial sample is represented in red while the full SDSS-DR7 sample is represented in grey. We estimated a stellar mass limit that depends on colour and redshift and above which our sample is complete in M_*. We notice that above that limit the fraction of quiescent galaxies does not evolve significantly. The methodology is described in Rodríguez-Puebla et al. (2020a, see also, van den Bosch et al. 2008).

structural properties. In contrast with previous studies, we investigate all these properties in a systematic way as a function of the distance of the galaxy from the SFMS ridge line. Particularly, we note that for CGs, $\nabla_{(g-i)}$, such systematic study has not been reported previously in the literature. CGs are key because they add another dimension to studying the properties of the stellar population as a function of galaxy's radius. In addition, unlike the previously mentioned papers, we study only central galaxies in order to avoid complex processes that exclusively affect satellite galaxies, which could hide important trends between the variables of interest. Finally, one of the main drivers of this paper is to understand the role that the global KS law plays in the interplay between SFR, mass, and structure/morphology.

In this paper, we show that SDSS galaxies follow a non-monotonic relationship between half-light/half-mass radius and specific SFR (sSFR) for a given stellar mass. We also observe a similar trend among other structural parameters, such as Σ_1, n, and CG. However, when studying the sSFR as a function of half-light radius, a negative monotonic relation emerges, consistent with the correct predicted relation from the global KS law, SFR$\propto R_e^{-0.28}$, when assuming the gas mass is constant for a given stellar mass. One of the major conclusion of this paper is that there is characteristic mass associated to the bend of the star-forming main sequence, $M_c = 2 \times 10^{10}$ M$_\odot$, below which structural parameters of central galaxies exhibit a notable change in behaviour across the SFMS. We find that galaxies with masses lower than M_c, as we move up across the SFMS at a fixed stellar mass, galaxies are compact, dense, with blue centres, and structurally similar to GV galaxies. In contrast, as we move down across the SFMS galaxies are larger and more discy with redder centres. We conclude that for low-mass galaxies, $M_* \leq M_c$, there are two mechanisms that could quench them. One is related to a change in morphology that happens fast, and the other is related to secular processes that happen more slowly. At higher masses, $M_* > M_c$, SFMS galaxies near the GV are structurally closer to those of the GV, as expected. In other words, galaxies changed their morphology before leaving the SFMS. Finally, we develop an empirical model based on the KS law that shows that the above trends are the result of the efficiency of the galaxies in transforming atomic into molecular hydrogen and forming stars.

This paper is organized as follows. Our methods are described in Section 2, including the SDSS galaxy sample used and how we divide the SFMS into subsamples based on sSFR. Section 3 describes the interplay we find between SFR, M_*, and galaxy structural parameters. Section 4 ranks the importance of various galaxy parameters in predicting the distance Δ_{MS} from the SFMS ridgeline. Section 5 describes our empirical model for the connection between R_e and SFR for a given $M*$. Section 6 discusses the empirical evidence for two paths for galaxy quenching. Section 7 discusses results and implications for the galaxy-halo connection. Finally, Section 8 summarizes our conclusions.

In this paper, we use the standard ΛCDM model with values of $\Omega_M = 0.3$ and $\Omega_\Lambda = 0.7$ with $h = 0.7$, an initial mass function (IMF) of Chabrier (2003) and R_e refers to the half-light radius along the semimajor axis. Finally, in this paper, the words *small* and *large* are reserved for the physical size of the galaxies while *low, high*, and *massive* are reserved for the stellar mass of the galaxy.

2 METHODS

2.1 The galaxy sample

In this paper, we use the catalogue of two-dimensional (2D) photometric Sérsic fits for the *r* band, reported in Meert, Vikram & Bernardi (2015) as well as catalogues for the *g*, and *i* bands reported in Meert, Vikram & Bernardi (2016) for galaxies in the SDSS Data Release 7. From these catalogues, we first select galaxies that have $m_r < 17.77$, $b/a > 0.5$, and a redshift range of $0.005 < z < 0.2$. In addition, we select galaxies with good total magnitudes and sizes, that is, we discard all the galaxies with flag bits 20 and above, see Meert, Vikram & Bernardi (2013) and Meert et al. (2015). For each galaxy in the catalogue, magnitudes and colours were $K + E$ corrected at a redshift rest-frame $z = 0$; for more details, see Rodríguez-Puebla et al. (2020a). Since we are interested in resolving the central kiloparsec of each galaxy in our sample, we found that the PSF radius of the SDSS (~ 0.75 arcsec) allows a redshift limit of $z < 0.0674$.

Fig. 1 shows the stellar mass (left) and effective radius (right) as a function of redshift of the full SDSS-DR7 data as grey dots. We follow Rodríguez-Puebla et al. (2020a, see also van den Bosch et al.

2008) to estimate a stellar mass limit that depends on colour and redshift, above which the sample is complete in stellar mass. We notice that by defining volume-limited subsamples above that limit, the fraction of quiescent galaxies does not evolve significantly with redshift (van den Bosch et al. 2008). In addition, we required that the half-light radius of every galaxy in the sample be larger than the SDSS PSF. The final selected galaxies we use for this work are shown as red dots.

We also use the SFRs tabulated from the GALEX-SDSS-WISE Legacy Catalog (GSWLC; Salim et al. 2016; Salim, Boquien & Lee 2018). The authors combined UV, optical, and 22 μm to derive robust SFRs by using the spectral energy distribution fitting distribution technique. In particular, their GSWLC-D2 and M2 data releases, which are the deepest and medium-deep catalogues, are suitable for studying local star-forming and quiescent galaxies. These catalogues represent ∼ 56 per cent of our sample. Since much of this paper focuses on studying the SFMS, we use their GSWLC-A2 all-sky sample to complement the remaining ∼ 44 per cent. We have checked that using only the GSWLC-D2 catalogue or the combined sample produces similar results. Therefore, we opted to use all three catalogues to increase the statistical power of our sample. Thus, our final sample of galaxies with reported SFRs consists of 39 873 galaxies objects.

Finally, this paper focuses on central (i.e. non-satellite) galaxies and the interplay between SFR, M_*, and morphology. To do so, we cross-correlated our catalogue with Yang et al. (2012, which represents an update to the Yang et al. 2007) group catalogue, to divide it into central and satellite galaxies. In this paper, we define central galaxies as those with the highest stellar mass in each group as done in Rodríguez-Puebla et al. (2015). Our final sample of central galaxies consists of 29 294 galaxies.

2.2 Structural parameters

In this section, we describe how we calculate the mass profile, half-mass radius R_*, the average mass density at 1 kpc, Σ_1, and CGs using data from the photometric catalogue from Meert et al. (2015, 2016) based on their Sérsic parameters for the g, r, and i bands. In order to calculate those quantities we must first derive the colour profiles. We make use of the Sérsic parameters given in the photometric catalogue and use their relationships to calculate surface brightness and luminosity profiles. The Sérsic (1963) surface brightness profile is defined as

$$I_\lambda(R) = I_{0,\lambda} \exp\left[-\beta_n \left(\frac{R}{R_{e,\lambda}}\right)^{1/n_\lambda}\right]$$
$$= I_{e,\lambda} \exp\left[-\beta_n \left\{\left(\frac{R}{R_{e,\lambda}}\right)^{1/n_\lambda} - 1\right\}\right], \quad (1)$$

where $I_{0,\lambda}$ is the central surface brightness, $R_{e,\lambda}$ is the radius that encloses half of the total light (typically referred to as the effective radius) along the semimajor axis of the galaxy, n_λ is the Sérsic index, $\beta_n = 1.9992n - 0.3271$, for $0.5 < n < 10$ (Capaccioli 1989) and $I_{e,\lambda}$ is the surface brightness at $R_{e,\lambda}$. The subscript λ represents the g, r, and i bands. The relation between $I_{e,\lambda}$ and $I_{0,\lambda}$ is given by

$$I_{e,\lambda} = I_{0,\lambda} e^{-\beta_n}. \quad (2)$$

We obtain the luminosity profile by integrating equation (1) over any given radius

$$L_\lambda(R) = 2\pi \int_0^R I_\lambda(R')R'\mathrm{d}R', \quad (3)$$

and the total luminosity L_λ by simply letting $R \to \infty$.[2] Notice that the luminosity profile for each g, r, and i bands were $K + E$ corrected as described at the beginning of this section.

In terms of the central surface brightness I_0 and the effective radius R_e the total luminosity is

$$L_\lambda = \frac{2\pi n_\lambda \Gamma(2n_\lambda)}{(\beta_n)^{2n_\lambda}} I_{0,\lambda} R_{e,\lambda}^2, \quad (4)$$

where $\Gamma(x)$ is the complete gamma function. At this point, from the Meert et al. (2015, 2016) catalogues we have constructed luminosity and magnitude profiles in the g, r, and i bands as well as colour profiles for $(g - i)$ and $(g - r)$. We use these photometric profiles to derived five stellar mass profiles, $M_*(R)$, from five different mass-to-light ratios following Rodríguez-Puebla et al. (2020a, see their appendix A, equation 34), where we also took the geometrical mean of the determinations to be our fiducial $M_*(R)$ profile and total M_*.

In this paper, we are interested in studying trends in the SFR–M_* plane, especially the deviations from the SFMS, with the morphostructural parameters of the galaxies as described in the Introduction section. In particular, the half-mass radius, R_*, at a given M_* (compactness) and the stellar surface mass density within 1 kpc, Σ_1, are quantities of interest that were not available for our sample. Thus, for each stellar mass profile described above we derived R_* and Σ_1 as described next. The half-mass radius R_* was computed by solving the following equation:

$$0.5 \times M_* - M_*(R_*) = 0, \quad (5)$$

and the stellar mass density within $R_1 = 1$ kpc, Σ_1, as

$$\Sigma_1 = \frac{M_*(R_1)}{\pi R_1^2}. \quad (6)$$

Similar to our stellar masses, we define our fiducial Σ_1 as the geometrical mean of the five different determinations while for R_* we compute the mean of the five estimations.

Finally, we define the CG for the $(g - i)$ optical colour as the differences in colour between the radius $R_{0.1} = 0.1 \times R_e$ and R_e, as done in Tortora et al. (2010),

$$\nabla_{(g-i)} = \frac{(g - i)_{R_{0.1}} - (g - i)_{R_e}}{\log(R_{0.1}/R_e)}. \quad (7)$$

In a similar way, we define $\nabla_{(g-r)}$. Notice that Meert et al. (2015, 2016) profiles were deconvolved by the point spread function of the SDSS. As will become clear later, in this paper, we focus mainly on SFMS galaxies. We found that the half-light radii for most of these galaxies have a median factor of ∼ 7 times larger than the PSF, implying that the Sérsic parameters are less affected by the PSF size. Additionally, we have checked that the CGs from Park & Choi (2005), who computed the CG in outer radii compared to ours, between 0.5 and 1 Petrosian radii, produce similar results to ours.

In this paper, we look specifically at the $(g - r)$ and $(g - i)$ optical colours due to the fact that these colours are primarily correlated with the temperature of the dominant stellar population, and therefore are mainly related to the age of the population rather than to the metallicity (Gonzalez-Perez, Castander & Kauffmann 2011). Thus, red colour implies older stellar populations while blue

---

[2]Notice that the some authors prefer to compute luminosity by truncating the fitted profiles up to 7.5 the half-light radius. The impact of truncating the luminosity impacts the stellar mass of massive galaxies, $M_* \gtrsim 10^{11.5}$ M$_\odot$, to an uncertainty smaller than ∼ 0.1 dex (Bernardi et al. 2017). Given that this uncertainty is small and most of our sample is below $M_* \sim 10^{11.5}$ M$_\odot$, we ignore this effect.
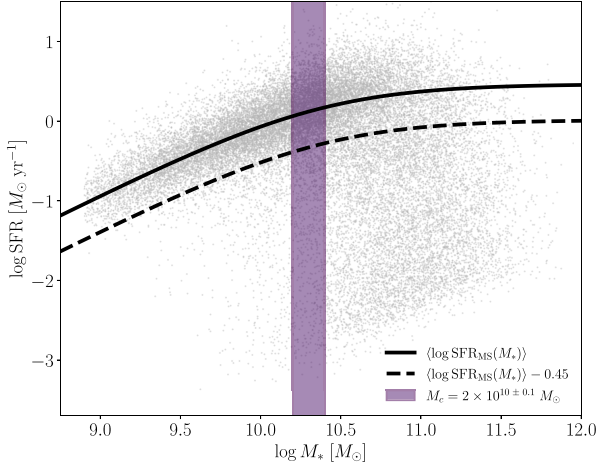
Figure 2. Star formation rate as a function of mass for our sample of central galaxies shown as grey dots. The black solid line represents our best-fitting relation to $\langle \log \mathrm{SFR_{MS}}(M_*) \rangle$ using a double power law function. The dashed line separates the SFMS from the remaining galaxies, including the GV and quiescent galaxies. Our analysis reveals a characteristic mass of $M_c = 2 \times 10^{10} \mathrm{M_\odot}$, above which the mean of the SFMS *bends*. This is represented as a shaded area of ± 0.1 dex width around M_c.

colours suggest more recent star formation. We define a galaxy to have a negative CG if the centre is redder as the outskirts turn blue. Positive gradients, therefore, imply galaxies with red outskirts and a bluer centre.

After studying both colours $(g - i)$ and $(g - r)$, we have concluded that there is no significant difference between the trends. CGs tend to be steeper in $(g - i)$ but the behaviour is always the same. In the next sections, we show only our results in $(g - i)$, although every calculation was also performed for $(g - r)$. In addition, we have repeated our results regarding the CGs but using those reported from the literature and found the same results (Morell, in preparation).

2.3 The star-forming main sequence

In this section, we describe how we separate the galaxy sample into several subsamples according to the distance to the mean SFMS.

As mentioned above, in this paper we use the SFRs from Salim et al. (2018). To obtain each subsample, we compute in an iterative way the mean M_*–SFR relation of SF galaxies, by initially using a slightly modified relation from Speagle et al. (2014) adapted to be closer to the mean SFMS of our data. Then, all the galaxies –0.45 dex below this relationship were excluded and this was our initial guess for the SFMS. We then performed a power-law fit to the SFMS for our trimmed sample. We use the latter fit to redefine our new sample of SFMS galaxies by using only the galaxies –0.45 dex above this relation. We repeat the above process until the parameters in the power-law fits do not change more than a tolerance of 10^{-3}. We note that the above is similar to the procedure described in Fang et al. (2018, see also Rodríguez-Puebla et al. 2020b). Using our sample of SFMS galaxies, we find that the best-fitting model that describes the mean relationship is given by the generalized equation proposed by Lee et al. (2015, see also, Leslie et al. 2020):

$$\langle \log \mathrm{SFR_{MS}}(M_*) \rangle = \log \mathrm{SFR_0} - \log \left[1 + \left(\frac{M_*}{M_0} \right)^\gamma \right], \tag{8}$$

where the best-fitting parameters are $(\mathrm{SFR_0}/M_\odot \mathrm{yr^{-1}}, \log(M_0/M_\odot), \gamma) = (0.464, 10.3815, -1.006)$. Fig. 2 presents the distribution of

Table 1. Selection of galaxy subsamples according to the distance of each galaxy to the SFMS.

Subsample	ΔMS bin (dex)
Highly star forming (HSF)	ΔMS > 0.25
Upper main sequence (UMS)	$0 < \Delta$MS < 0.25
Lower main sequence (LMS)	$-0.25 < \Delta$MS < 0
Bottom of the main sequence (BMS)	$-0.45 < \Delta$MS < -0.25
Green valley (GV)	$-1 < \Delta$MS < -0.45
Quiescent (Q)	ΔMS < -1

SFRs as a function of mass for our sample of central galaxies, along with the best-fitting relation to equation (8). One crucial observation is the characteristic mass of M_*, beyond which the mean of the SFMS *bends*. This bend in the SFMS has been a subject of discussion in previous studies (e.g. Salim et al. 2007; Whitaker et al. 2014; Lee et al. 2015; Schreiber et al. 2015; Leslie et al. 2020), with similar mass ranges to what we report here. Below M_c the SFMS follows a power law SFR $\propto M_*^{0.85}$, whereas at higher masses the SFMS flattens out, with SFR$(M_*) \sim$ const. When converting M_0 to a dark matter halo mass, it has been noted to be consistent with the halo mass scale $M_{\mathrm{vir}} \sim 10^{11.8}$, above which virial shock formation occurs, leading to a reduction in available cold gas in galaxies (Daddi et al. 2022). We will revisit this point in Section 6. Due to the significance of this characteristic mass within the SFMS, we will utilize it to examine changes along the SFMS. Henceforth, we define the characteristic mass centred at $M_c = 2 \times 10^{10} \mathrm{M_\odot}$ with a conservative uncertainty of ± 0.1 dex around it due to random errors in stellar mass (Conroy et al. 2013), and represent it in the relevant figures as a shaded area.

Once we have characterized the mean SFMS, equation (8), the next step in our programme is to define nominal subsamples according to the distance of each galaxy from the mean SFMS relationship:

$$\Delta_{\mathrm{MS},i} = \log \mathrm{sSFR}_i - \langle \log \mathrm{SFR_{MS}}(M_*) \rangle, \tag{9}$$

where sSFR_i is the observed sSFR for the ith galaxy.

Table 1 summarizes the definition of each subsample. Here, we will assume that the SFMS has a standard deviation of the order of $\sigma \sim 0.25$ as has been found previously in the literature (e.g. Salim et al. 2007; Speagle et al. 2014). The subsamples are as follows: (1) highly star-forming (HSF); these are galaxies 1σ above the mean SFMS that may include starburst galaxies, we note, however, that starburst galaxies do not represent a large fraction of this galaxies; (2) upper main sequence (UMS): these are galaxies above the mean SFMS but within the 1σ distribution; (3) lower main sequence (LMS): these galaxies correspond to those that are below the mean SFMS and within the 1σ distribution; (4) bottom of the main sequence (BMS) corresponds to those galaxies that are below the 1σ distribution but still at a distance above -0.45 dex below the mean SFMS; these galaxies are presumably approaching to the distribution of GV galaxies, or quiescent galaxies by fading their SF. GV galaxies are those between 0.45 dex and 1 dex below the mean SFMS, while quiescent galaxies correspond to all galaxies that are 1 dex below.

3 THE INTERPLAY BETWEEN SFR, M_*, R_e, AND STRUCTURAL PARAMETERS

The goal of this paper is to study whether there is, at fixed M_*, a correlation between the SFR and the structure of the galaxies. As discussed in the Introduction section, previous authors have shown that, broadly speaking, there is a positive correlation between SFR

and galaxy structure (size, density, etc.), when galaxies are divided into two broad populations: star forming and quiescent. Here, we diverge from the previous studies in two ways:

(i) By studying the SFR and structure as a function of the distance from the main SFMS (Table 1).

(ii) And by studying this from the perspective of the Kennicutt−Schmidt law, which implies that for a fixed M_* and gas mass, small and compact, high central density galaxies are more star forming (see Section 5).

As such, we will not only describe the quantitative/qualitative aspects of the structural properties in the SFR–M_* plane, but also gain insight into the underlying physics of galaxy evolution by understanding how gas is transformed into stars from the global KS law. This will be discussed in more detail in Section 5.

On the other hand, it is not the SFR–radius relation that we study here, but rather Δ_{MS} versus radius. Given that the radius (either the half-light or half-mass radius) is one of the quantities directly related to the KS law (see Section 5 below and also Lin et al. 2020), we will spend more time below discussing the SFR–radius relationship than the other relations.

Finally, the best way to understand how the morphostructural properties of galaxies are related to their location in the sSFR–M_* plane is by studying the locations of the subsamples defined in Table 1 in the size–mass, CG–mass, Σ_1–mass, and Sérsic index–mass relationships. More precisely, for each of our Δ_{MS} subsamples, we compute its mean relations in those planes. In addition, given that the global KS law involves the radius, we also study the continuous distribution of sizes as a function of the distance from the SFMS for a given M_*. Notice that the dependence with stellar mass is removed as our selection depends only on the distance to the SFMS in such a way that, when describing our results, the differences between the subsamples, if there are any, should be interpreted for a given M_*.

3.1 The dependence of R_e as a function of the SFR: HSF low-mass galaxies are compact

Figs 3 and 4 present one the main results of this paper by showing how the mean sSFR-M_* relationships for each of the Δ_{MS} subsamples defined above (see Table 1) are projected into the R_e-M_* relation. The right panel of Fig. 3 shows the mean R_e of these subsamples as a function of mass. On average, the sizes of the SFMS galaxies are larger than those of the GV and quiescent galaxies. The sizes of the GV galaxies are also larger than those of the quiescent galaxies. These trends are consistent with results previously reported in the literature (Omand et al. 2014; van der Wel et al. 2014; Lange et al. 2015, and more references therein). Naively, at this rough level of segregation one could conclude that, on average, more extended galaxies should be more star forming than compact galaxies, for a given stellar mass. Does this imply a monotonic relationship, except for some random scatter, between size and sSFR? According to the results shown in the right panel of Figs 3 and 4, this is not the case and the answer is mass dependent.

If we look at galaxies with stellar masses below $M_c = 2 \times 10^{10} M_\odot$, we find that, on average, the sizes of the HSF galaxies, $\Delta_{MS} > 0.25$ dex, are smaller than any other counterpart in the SFMS, i.e. galaxies with $-0.45 < \Delta_{MS}[\text{dex}] < 0.25$. For example in Fig. 4, in the first mass bin it goes from $R_e \sim 2.5$ kpc at $\Delta_{MS} \sim -0.3$ dex to $R_e \sim 1.3$ kpc at $\Delta_{MS} \sim 0.5$ dex. In other words, sizes have decreased nearly a factor of ~ 2 across the SFMS. In the next two mass bins, we found factors of ~ 2 and ~ 1.5, respectively. All these results are consistent with Wuyts et al. (2011). Interestingly, HSF galaxies

are smaller than GV galaxies but somewhat larger than quiescent galaxies. This observation suggests that HSF galaxies with masses less than M_c may serve as the progenitors of GV and quiescent galaxies (see also Wuyts et al. 2011); further discussion on this in Section 6. Additionally, UMS galaxies are, on average, smaller than LMS and BMS galaxies for masses below $M_* \sim 10^{10} M_\odot$ and exhibit similar half-light radii to GV galaxies. This further supports the notion that galaxies above the SFMS, particularly HSF galaxies, are structurally closer to galaxies below the SFMS, especially the GV galaxies.

For galaxies more massive than M_c but smaller than $M_* \sim 10^{11} M_\odot$, we find that HSF and BMS galaxies are similar in size. In addition, BMS and HSF are structurally closer to GV galaxies. In contrast UMS and LMS galaxies are more extended and larger than BMS and HSF. Above $M_* \sim 10^{11} M_\odot$ the differences are not that obvious and the size–mass relations of all our subsamples seem to converge to the same relationship.

In Fig. 4, we now look at the distribution of R_e as a function of the distance from the MS, Δ_{MS}, in different mass bins. We show the mean value of this relationship for each subsample at each mass bin with red solid lines; the red shaded area represents the error of the mean. As noticed in Fig. 3, galaxies that are in the lower SFMS (LMS) are larger, on average, while the ones that have the highest SFRs (HSF) tend to have smaller radii. This is consistent with the results obtained by Wuyts et al. (2011, see also Lin et al. 2020 who found weaker trends). This trend is most obvious in low-mass bins. In the case of more massive, the difference in size for each subsample begins to disappear. We also highlight that for galaxies smaller than $M_* \sim 10^{10} M_\odot$ the mean largest size is reached closer to the GV, vertical black line in Fig. 4.

If we compute the slopes of $R_e \propto \text{SFR}^{-\alpha}$ for galaxies with $\Delta_{MS} > 0$, which are the ones that clearly display trends between sizes and SFR, we find $\alpha \sim 0.4, 0.4, 0.3, 0.2,$ and 0 in each mass bin, confirming the trends described above. Notably, these slopes are shallower than what would be expected by the global KS law[3] (with a slope of $n = 1.42$), specifically $R_e \propto \text{SFR}^{-1.19}$. It is important to note that the SFRs vary from galaxy to galaxy, and shallower slopes can be the result of inverting the KS without considering this source of scatter. The blue solid line in each panel represents the value $\langle \Delta_{MS} \rangle$ as a function of R_e. Consistent with our previous results, we also find a negative monotonic trend between SFR and size. We report slopes of $\beta \sim 0.3, 0.3, 0.4, 0.2,$ and 0.1 for $\text{SFR} \propto R_e^{-\beta}$ in each mass bin. Again, these slopes are shallower than what would be expected by the global KS law, $\text{SFR} \propto R_e^{-0.84}$, black dotted line. Therefore, the shallower slopes found in the inverted relation cannot be solely attributed to the scatter in SFRs. We will revisit this point in Section 5.

So far we have studied our results based on the half-light radius. At this point, an obvious question is whether our results are biased due to the CG in galaxies.[4] For that reason, the next step is to investigate if our main conclusions are consistent when analysing the half-mass radius (Fig. 5).

Similarly to the half-light radius, we again find that, on average, the half-mass radii of SFMS galaxies are larger than those of the GV and quiescent galaxies. The sizes of the GV galaxies are larger than

---

[3] As described in the Introduction Section, we assumed that the gas mass is the same for a given M_* as in Lin et al. (2020).

[4] IMF-driven gradients could also potentially bias our results (e.g. Bernardi et al. 2023). Corrections due to effects of IMF gradients are out of the scope of this paper.
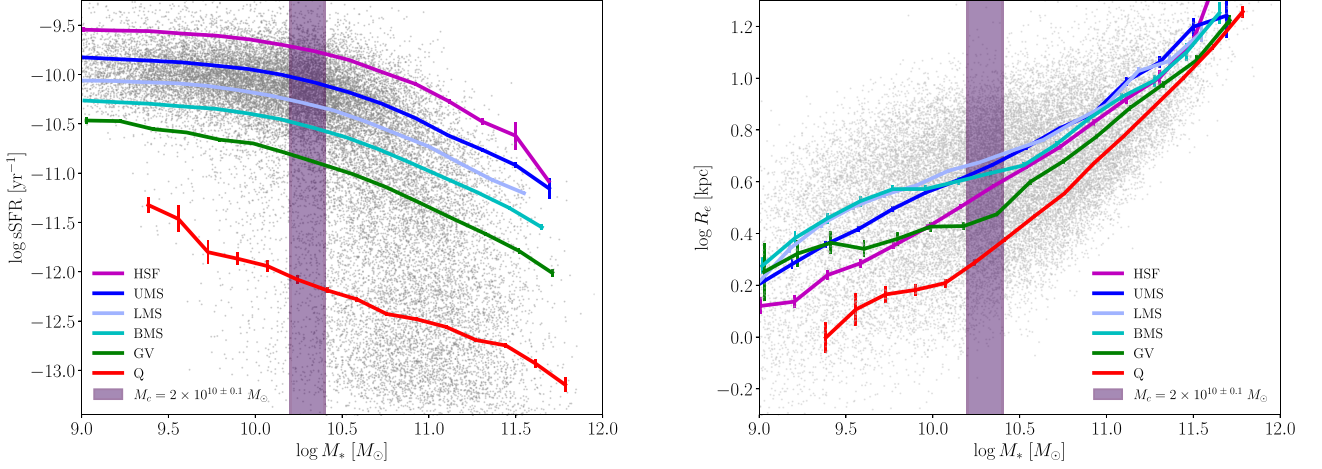
Figure 3. From left to right, we show sSFR and R_e as a function of mass. On each panel, every coloured line represents the average trend for each subsample of central SFMS galaxies: Highly star-forming (HSF), UPS, LMS, bottom main sequence (BMS), GV, and quiescent. Left panel: the sSFR as a function of M_*. In this panel, the mean for each subsample is shown for clarity and reference. Right Panel: r-band half-light radius versus stellar mass. Note that HSF galaxies have smaller R_e than UMS, LMS, and BMS (i.e. all the other SF subsamples). In fact, at masses below $M_* < 10^{9.5}$ M$_\odot$, HSF galaxies have an R_e almost identical to that of GV galaxies. In general, the average R_e of HSF stays parallel to the average of GV galaxies for all masses. At $M_* > 10^{10.5}$ M$_\odot$, the half-light radii of all subsamples begin to converge. Note that these high-mass HSF galaxies now resemble BMS galaxies in size. However, the R_e of HSF still remains only greater than GV and quiescent galaxies even at high masses.
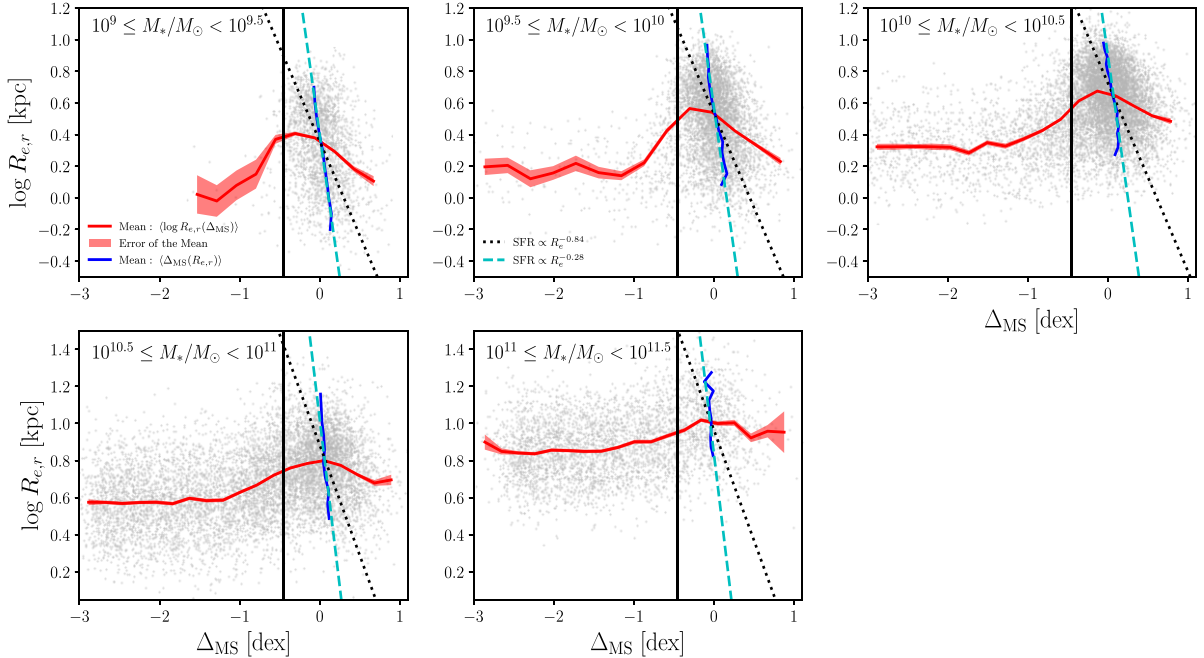
Figure 4. Galaxy half-light radius as a function of the distance above or below the main sequence, Δ_{MS}, for five different stellar masses. Each panel represents the distribution of galaxies at a given mass bin (grey dots). The solid red lines represent the mean $\langle \log R_{e,r} \rangle$ as a function of Δ_{MS} while the light red shading is the error of the mean. The vertical black line at $\Delta_{MS} = -0.45$ dex separates GV and quiescent galaxies from the SFMS. The blue line in each panel shows the mean $\langle \Delta_{MS}(R_{e,r}) \rangle$ for SFMS galaxies which are the ones expected to follow the global KS law. The black dotted lines show the expected relationship between size and SFR from the global KS law; SFR $\propto R_e^{-2(n-1)}$ if $n = 1.42$ then SFR $\propto R_e^{-0.84}$ or $R_e \propto$ SFR$^{-1.19}$. In each panel from low to high masses, we find slopes of $\alpha \sim 0.4, 0.4, 0.3, 0.2$ and ~ 0 for $R_e \propto$ SFR$^{-\alpha}$ and galaxies with $\Delta_{MS} > 0$, and, $\beta \sim 0.3, 0.3, 0.4, 0.2$ and ~ 0.1 for SFR $\propto R_e^{-\beta}$ and SFMS galaxies. These slopes might imply that the global KS law is inconsistent with the expected trends in this plane. As we will show in Section 5, the correct trends, predicted by taking into account that the global KS law is defined within a star-forming region, imply a shallower relation of the form SFR $\propto R_e^{-0.28}$, consistent with our observed slopes. This is represented by the cyan dashed lines.
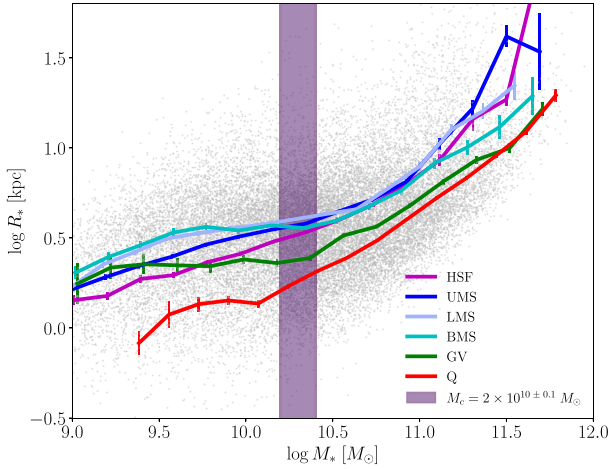
Figure 5. Half-mass radius R_{e*} as a function of stellar mass. Every coloured line represents the average trend for each subsample of central SFMS galaxies, see Table 1. At low masses, BMS, and LMS galaxies tend to have the largest R_{e*}. Low-mass HSF galaxies reproduce a very similar trend to that of GV galaxies. Quiescent and GV galaxies have the smallest half-mass radius at any given mass. Notice that HSF galaxies have radii smaller than all SF subsamples below $M_* \sim 2 \times 10^{10} \mathrm{M}_\odot$. Above $M_* \gtrsim \sim 2 \times 10^{10} \mathrm{M}_\odot$, GV galaxies are, on average, similar to quiescent galaxies and HSF are no longer as compact as in lower masses. BMS galaxies have the smallest R_{e*} of all SF subsamples followed closely by HSF galaxies.

those of the quiescent galaxies, particularly at low masses. The major differences with the half-light radius results occur when dissecting the size–mass relation into different subsamples by SFR.

We begin by describing low-mass galaxies, $M_* \lesssim M_c$, from Fig. 5. We observe once more that HSF galaxies are, on average, smaller than all other star-forming galaxies and exhibit radii closer to the average of GV galaxies. Notably, for masses below $M_* \sim 3 \times 10^9 \mathrm{M}_\odot$, HSF galaxies appear even smaller than GV galaxies. Similarly, UMS galaxies are smaller than LMS and BMS galaxies, displaying greater resemblance to GV galaxies. LMS and BMS have similar sizes. Below $M_* \sim 3 \times 10^9 \mathrm{M}_\odot$, on average, BMS galaxies are the largest galaxies of all the subsamples.

We now turn our analysis to galaxies more massive than M_c. For those galaxies, we observe that massive BMS and HSF galaxies are, on average, smaller than any other SF subsamples. However, all SFMS galaxies appear to have very similar average sizes. Additionally, while GV galaxies exhibit larger half-light radii to those of quiescent galaxies, their half-mass radii at higher masses are also comparable to those of quiescent galaxies.

In general, we find that the main conclusions obtained for the half-light radius versus M_* are also applicable when analysing the half-mass radius instead (see Fig. 5). None the less, the *trends are weaker*. Therefore, the answer to our question of whether our results are biased due to the CGs of the galaxies is no, although we did find small differences between the two radii that could potentially be attributed to CGs. In the following section, we will analyse CG as a function of mass and distance to SFMS galaxies.

Finally, we have checked that our main conclusions were recovered when using r−band half-light radii from single Sérsic fits of Simard et al. (2011) as well as when using their sizes for a two Sérsic fit component instead of Meert's. Additionally, we have checked that when using the Petrosian radius from Park & Choi (2005) our conclusions remain unchanged (Morell et al., in preparation).
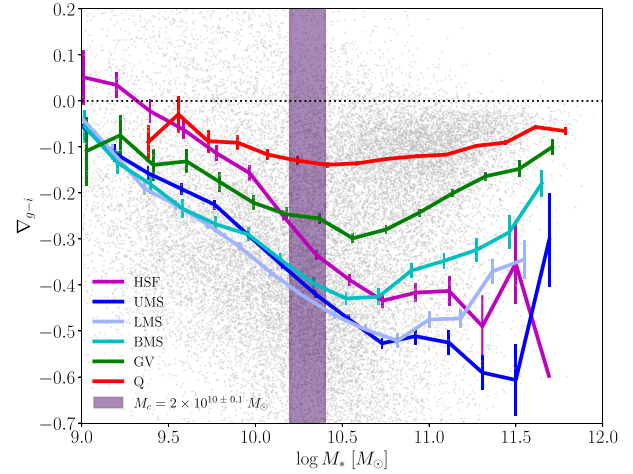
Figure 6. Average CG $\nabla_{(g-i)}$ for each central galaxy subsample of SFMS galaxies (see Table 1). Negative gradients represent galaxies with redder centres than their outskirts. Positive gradients represent bluer centres. Quiescent galaxies have, on average, near-zero CGs at all stellar masses. From GV galaxies to UMS galaxies, the negative CGs get steeper as the SFR increases. However, note that HSF galaxies do not have the most negative gradients. Especially at low masses, HSF galaxies have near-zero CGs, and the trend remains above that of the GV galaxies below $M_* \sim 10^{10} \mathrm{M}_\odot$. LMS galaxies show the steepest CG at low masses, while UMS galaxies display the steepest gradients at high masses.

Furthermore, we have questioned ourselves whether our SFRs are another source of spurious trends. Considering that the SFRs from Salim et al. (2018) were based on WISE data, it is possible that certain galaxies, especially in their outer regions, in particular in massive galaxies, may exhibit shallower *WISE* colours, potentially leading to underestimated SFRs. By employing alternative empirical dust-corrected SFR indicators based on spatially resolved IFU spectroscopic data from the Mapping Nearby Galaxies at APO (MaNGA) survey (Bundy et al. 2015), we have repeated Fig. 4 and found that this new SFR estimator replicated the same results (Faber et al., in preparation). Therefore, the trends described in this section remain robust independently of the sizes and SFRs indicators used in this work. On the other hand, trends weaken at high masses and therefore the above does not change our general conclusions.

3.2 The CGs: low-mass HSF galaxies tend to have bluer centres

Fig. 6 shows the mean CG $\nabla_{(g-i)}$–M_* relation divided into our six sSFR subsamples. We notice that our CGs are consistent with the results found by previous authors (e.g. Tortora et al. 2010; Gonzalez-Perez et al. 2011; Pan et al. 2015), i.e. CGs depend on mass and SFR; star-forming galaxies have on average more negative CGs as they get more massive, while quiescent galaxies have approximately zero CGs. Recall that negative CGs correspond to redder centres and bluer outskirts, while positive gradients correspond to bluer centres and redder outskirts. As described in Section 2.2, bluer colours will be associated with younger ages, and thus, with recent episodes of star formation. We now study in detail the differences between our SFR divisions.

In the case of low mass SFMS, $M_* \lesssim M_c (= 2 \times 10^{10} \mathrm{M}_\odot)$, our results show that as the SF increases, on average, CGs are less negative. Indeed, the CGs of HSF are consistent with zero or even positive values for the lowest masses. HSF galaxies have a similar trend to the GV galaxies at low masses, below $M_* \sim 10^{10} \mathrm{M}_\odot$,
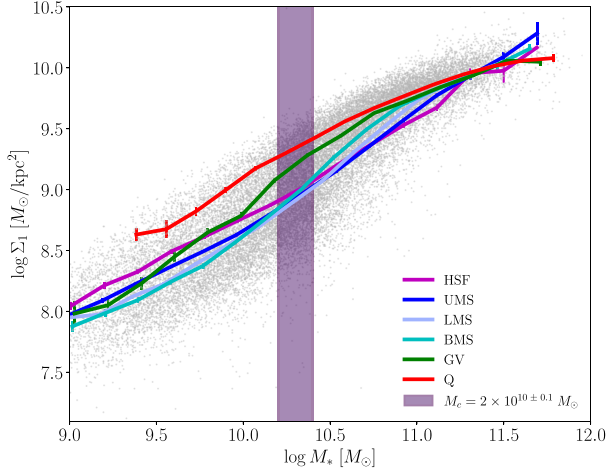
Figure 7. Average central mass density Σ_1 as a function of mass for each subsample of SFMS galaxies (see Table 1). As mass increases, the central density increases as well for all galaxies. Predictably, we see quiescent galaxies being the most centrally dense at any given mass. Something interesting to note is that HSF galaxies at very low masses have the same central mass density as GV galaxies. At $M_* \sim 10^{9.5}\,M_\odot$, GV galaxies become the second most centrally dense and HSF galaxies continue to decrease their central density with respect to the other subsamples as they reach higher masses. At $M_* \sim 10^{11.5}\,M_\odot$ however, all galaxy subsamples converge in central mass density.

both approach to positive gradients. We highlight that similar to the result seen in the half-light and half-mass–M_* relations, HSF and GV galaxies remain similar in their properties. UMS, LMS and BMS have similar negative CGs.

At high masses, $M_* \gtrsim M_c$, BMS galaxies have less negative gradients compared to other SFMS galaxies. In fact, for masses $M_* > M_c$, BMS CGs are only more negative than GV and quiescent galaxies. We notice that for almost all masses $\lesssim 10^{11}\,M_\odot$, LMS and UMS resulted in similar CGs.

Our results point out that while being within the 1σ SFMS the CG of the galaxies are mainly negative. However being a low mass and HSF galaxy, necessarily implies having a radial difference in the stellar population properties, in the direction of having a bluer centres. Also, high-mass BMS galaxies tend to have flatter CGs. Next, we investigate how the internal structure of the galaxies is correlated with the above results.

3.3 Central mass density and Sérsic index: low-mass HSF galaxies are denser

To look more deeply into the results presented above, that is, the non-monotonic behaviour of size and CGs with SFRs, we now look at the Σ_1-M_* relationship. In the past, Σ_1 has been used as a surrogate for the bulge (and its type) of the galaxy and thus of the central SMBH (Fang et al. 2013; Chen et al. 2020; Luo et al. 2020). The next step of our programme is to study the Σ_1-M_* relationship.

Fig. 7 shows the mean Σ_1-M_* relationships for each subsample. We find that, on average, quiescent and GV galaxies are the most centrally dense. In more detail, for low-mass galaxies, $M_* \lesssim M_c$, we find a similar trend to all our previous results: galaxies above the SFMS exhibit a trend more similar to GV galaxies, on average, than those below the SFMS. In other words, SFMS galaxies get, on average, more centrally dense as their SFR increases at low masses. Indeed, BMS galaxies are the least centrally dense of all subsets
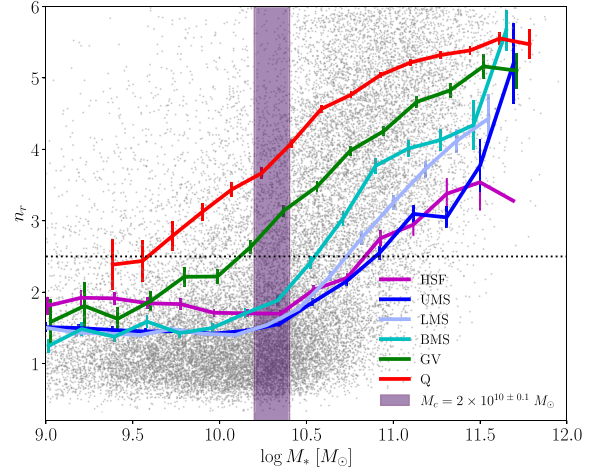
Figure 8. Average Sérsic index n_r for each central galaxy subsample of SFMS galaxies (see Table 1). Notice the same pattern of galaxies with masses below $M_* \sim 2 \times 10^{10}\,M_\odot$ in HSF galaxies being, on average, similar to GV galaxies, with a Sérsic index of $n_r \sim 2$. Above this mass, BMS galaxies have the largest n_r of all the SF subsamples, while UMS and HSF have the lowest.

at low masses. For more massive galaxies, $M_* \gtrsim M_c$, the opposite happens as mass increases. BMS and LMS galaxies increase their central density. Near $M_* \sim 10^{11}\,M_\odot$, the central density increases for all subsamples as sSFR decreases. Finally, above $M_* \sim 10^{11}\,M_\odot$ all galaxies have similar values of Σ_1.

Fig. 8 shows the relationship between Sérsic index in the r band, n_r, and M_*. For galaxies with masses below $M_* \sim M_c$, we have persistently observed a pattern in which HSF galaxies are structurally similar to GV galaxies, with both exhibiting a Sérsic index of $n_r \sim 2$, while all other SFMS subgroups have more similar and lower Sérsic index, $n_r \sim 1.5$. At higher masses, $M_* \gtrsim M_c$, BMS galaxies have the largest Sérsic index of all the SFMS subgroups while the UMS and HSF galaxies have the lowest values. As we move to higher masses ($M_* \gtrsim M_c$), we observe that the BMS galaxies have the largest Sérsic index of all the SFMS subgroups, while the UMS and HSF galaxies exhibit the lowest values. This trend suggests that as galaxies become more massive, their light profiles become more centrally concentrated as we descend across the SFMS, contrary to the results at lower masses.

While the structural parameters studied in this section provide insights into their correlation along the SFMS, the above analysis does not indicate their ranking of importance as predictors for SFRs at a given M_*. We will address this question in the next section.

Finally, while in this section we study mean trends as a function of mass and distance from the MS, we have checked that all the above results remain very similar when using medians instead of means. We do not show medians for the sake of the space but they can be downloaded here.[5]

4 WHAT MATTERS FOR PREDICTING $\Delta_{\rm MS}$ OF SFMS GALAXIES?

So far, we have analysed the behaviour of R_e, Σ_1, n_r, and $\nabla_{(g-i)}$ as a function of the distance from the MS, $\Delta_{\rm MS}$. We aim now

[5]https://drive.google.com/drive/folders/1vu30ofFeL7lBatYBVWSDjf1lcey vnaWQ?usp = sharing

to understand which among these features is the most relevant in inferring Δ_{MS}. In this way, not only, we can confirm the results already found, but we can also provide a quantitative estimate of how each individual physical property is related to the measure of distance from the SFMS. To address this question, we exploit the so-called Generalized Additive Models (GAMs) with pairwise interactions, GA^{2}Ms, a machine learning (ML) technique that allows inferring an unknown variable and expressing it as a composition of functions. The original GAMs were proposed by Hastie & Tibshirani (1990). A GAM is an additive model able to capture the relevance of different predictive features, using a composition of smooth functions, usually splines. The idea of a GAM is quite simple: it allows connecting some predictors to a dependent variable. A GA^{2}M improves the accuracy of a classical GAM, accounting for the cross-correlations between two features (Lou et al. 2013; Caruana et al. 2015).[6]

To train our GA^{2}M, we rely on the ML method called Explainable Boosting Machine (EBM), a C++/PYTHON implementation of the GA^{2}M algorithm. EBM is part of the InterpretML library (Nori et al. 2019), an open-source PYTHON-based package of different ML methods. The big plus of EBM is that it has very high accuracy in the inference, comparable with those of random forest or boosted tree techniques, but, at the same time, is very informative like classical linear or logistic regressions. In EBM, the link function g receives the summation of each shape function and provides an estimate of the target. The role of each feature in the inference is sorted according to the overall importance it has in making the final prediction.[7]

We consider here the SFMS subsample discussed in the previous Section 2.3 by limiting the analysis only to galaxies above the SFMS (which comprises HSF and UMS) and below (which comprises LMS and BMS). Each subsample is then subdivided into two stellar mass bins: $9 \leq \log(M_*/M_\odot) < 10.3$ and $\log(M_*/M_\odot) \geq 10.3$. The main motivation for having two mass bins is simply because, in the preceding sections, we notice a change in the behaviour between structural properties with Δ_{MS} if galaxies are above or below $\sim M_c$. In the following, we show the results of the analysis not accounting for the terms due to the pairwise interactions, so reducing from a GA^{2}M to a classical GAM (hence removing the second-order term in equation 10), because we found their contribution negligible. In Table 2, we list the parameters used to train EBM.

---

[6]Briefly, assume a given data set $\mathcal{D} = (\mathbf{x}_i, y_i)_1^N$, where N is the size of the data set, $\mathbf{x}_i = (x_{i,1}, ..., x_{i,p})$ is the set of p features, while y_i is the target quantity to be inferred. By indicating with x_j the jth variable within the space of features, a GA^{2}M can be expressed as

$$g(E[y]) = y_0 + \sum_j f_j(x_j) + \sum_{j \neq k} f_{jk}(x_j, x_k). \qquad (10)$$

In equation (10), y is the dependent variable of the problem, $E[y]$ denotes the expected value, and g is the so-called *link function*. For each f_j or f_{jk}, namely the 1D and 2D*shape functions*, respectively, $E[f_j] = E[f_{jk}] = 0$. The non-parametric nature of the shape functions ensures that their shapes are totally determined by the data, guaranteeing a degree of flexibility in the estimate of the model.

[7]To determine the importance of each feature (and of pairwise interactions, if considered), the method computes the mean of the absolute values of the corresponding shape function. For each 1D shape function, the x-axis spans over the range of the related feature, while the y-axis corresponds to the so-called *score*, a quantity in units of the dependent variable y to be added to make the final inference of y considering all the other functional terms as well. Analogously, in the 2D shape functions the x- and y-axes correspond to two features, while the score is a third quantity, usually represented as a coloured heatmap.

Table 2. Parameters used to train the EBM method implemented in the InterpretML package (Nori et al. 2019).

Parameter	Description	Value
binning	Binning method	*quantile*
max_bins	Maximum bin number for f_j	256
interactions	Number of pairwise interactions	0
outer_bags	Number of outer bags	100
inner_bags	Number of inner bags	100
validation_size	Validation sample size for boosting	15 per cent
learning_rate	Learning rate for boosting	0.01

Fig. 9 shows galaxy properties according to the rank ordering of their importance to predict sSFRs for each subsample. The numbers indicated in the rectangles show the *mean absolute score* of each property: the higher the value, the more relevant the property is for predicting SFR. We clarify here that the absolute value of the score does not express the degree of correlation between two quantities, such as the Pearson correlation coefficient, but it gives an overall quantitative measure of how much the quantity to be inferred, Δ_{MS} in the case analysed, varies as each physical property taken into consideration varies. In general, we do not see strong differences between the structural properties used in this work. In detail, however, for low-mass galaxies above the SFMS Σ_1 (become more centrally denser) is more important followed by the CG. For galaxies below the SFMS, again Σ_1 is on the top but this time followed by the Sérsic index. At higher masses, galaxies above the SFMS R_e (being compact) is more important, while for galaxies that are below the SFMS the Sérsic index is more important. The former is followed by the CG while the latter is followed by Σ_1.

As we have seen in the previous sections, the structural properties Σ_1, n_r, and R_e display similar behaviours as a function of Δ_{MS} for a given M_*. The above is indeed expected since they are correlated through the Sérsic profile. Therefore, one could question whether the results shown here are robust since Σ_1, n_r, and R_e are expected to be redundant variables. Note, however, that redundant variables are expected to have similar scores. While Fig. 9 shows that the trends are weak, we notice that indeed there are clear differences between galaxy properties ranked first and second. In Appendix A, we present further information from EBM, such as the correlation matrix, the one-dimensional (1D)-shape score functions, and the results of the analysis performed on a set of test samples. All these figures confirmed the results obtained in the preceding sections, but using an alternative technique: as we move higher from the mean of the SFMS, lower mass galaxies are smaller, more centrally concentrated, and have bluer centres; as we move lower from the mean of the SFMS, lower mass galaxies are more extended with redder centres. All these trends are described by the shape functions in Appendix A which show the variation of Δ_{MS} with each property, for each subsample. For completeness, we also provide the correlation matrices between the various quantities involved in our analysis.

5 THE INTERPLAY BETWEEN THE RADIUS, SFR AND THE GAS CONTENT FOR A GIVEN M_*

In this paper, we find empirical evidence indicating that the effective radius (R_e, see also Wuyts et al. 2011) and the structural properties, namely Σ_1, n_r, and $\nabla_{(g-i)}$, exhibit on average a non-monotonic behaviour as a function of their distance to the SFMS Δ_{MS}. Notice
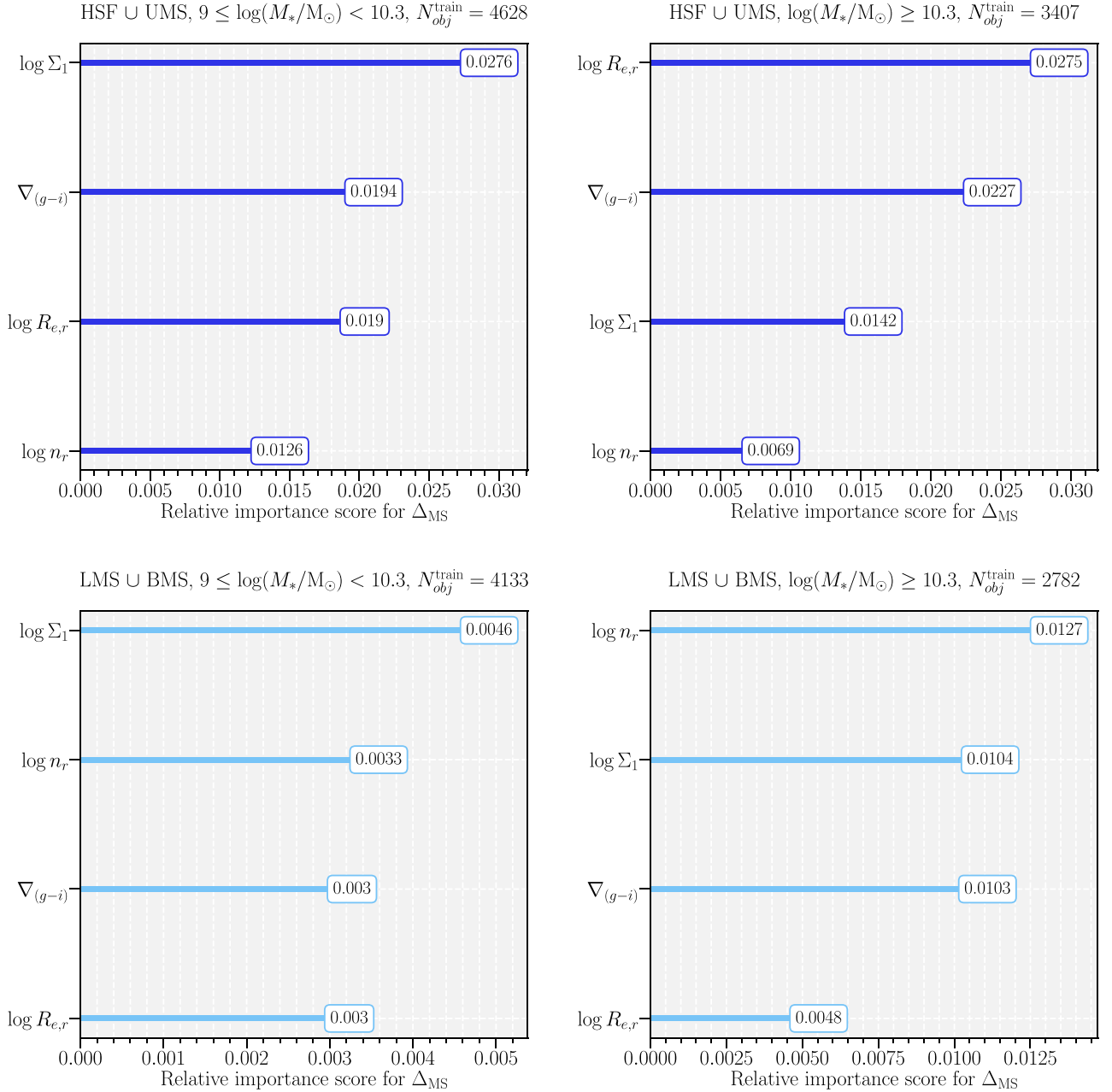
Figure 9. Relative importance scores for Δ_{MS} of $\log \Sigma_1$, $\nabla_{(g-i)}$, $\log R_{e,r}$, and $\log n_r$. The top panels refer to SF galaxies above the SFMS (i.e. HSF and UMS), while the bottom panels refer to SF galaxies below the SFMS (i.e. LMS and BMS). For each galaxy subset, we show the results at $9 \leq \log(M_*/\mathrm{M}_\odot) < 10.3$ (left panels) and at $\log(M_*/\mathrm{M}_\odot) \geq 10.3$ (right panels). The length of each bar is obtained by computing the mean absolute value of the corresponding 1D shape function.

that it is anticipated that R_e shows similar trends for a given mass, along with Σ_1 and n_r, as these parameters are statistically correlated.

As discussed in the Introduction section, assuming that the gas mass is constant for a given M_* (indeed, M_g correlates tightly with M_*; see e.g. Calette et al. 2018), the global KS law implies a negative monotonic relation between size and SFR. That is, more compact galaxies and higher density galaxies are more star forming, SFR $\propto R_e^{-0.84}$ or $R_e \propto$ SFR$^{-1.19}$. This is not what we observe on average in Fig. 4 and instead shallower slopes, ~ -0.3, are found for the former relation. Is this an indication that the relationship between size and

SFR for a given mass is inconsistent with the global KS law? In this Section we develop a phenomenological model based on the global KS law to empirically understand the above and the observed trends along the SFMS described in the preceding Sections.

Our discussion starts by introducing the global KS law for the total gas mass[8] (Kennicutt 1998b; Kennicutt & Evans 2012; de los Reyes & Kennicutt 2019). This law establishes a connection between

---

[8]Notice that the total gas mass from the original Kennicutt paper is given by $M_{\mathrm{gas}} = M_{\mathrm{HI}} + M_{\mathrm{H_2}}$, i.e. no correction for helium and metals were made.

a global characteristic gas surface density and a global characteristic surface SFR,

$$\Sigma_{SFR} = A_{KS}\Sigma_{gas}^n, \tag{11}$$

where the normalization factor has a value of $A_{KS} = 2.5 \times 10^{-4} \pm 0.7\,M_\odot yr^{-1}kpc^{-2}$ for a Salpeter (1955) IMF and the exponent $n = 1.42$ (Kennicutt 1998b, for a recent determination but similar to the original one, after accounting differences in IMF, see de los Reyes & Kennicutt 2019). The global surface density quantities in the KS law are derived by computing the mass in gas and the SFR contained within a star-forming region of radius R_{SF} encompassing approximately ~ 95 per cent of the H$_\alpha$ flux (de los Reyes & Kennicutt 2019), $\Sigma_{gas} = M_{gas}(< R_{SF})/\pi R_{SF}^2$ and $\Sigma_{SFR} = SFR(< R_{SF})/\pi R_{SF}^2$. By definition $SFR(< R_{SF}) = 0.95 \times SFR$. Notice that the star formation radius can be, on average, as large as a factor of ~ 1.7 compared to the half-light radius R_e for SFMS galaxies, but it is a trend that can vary with mass (see Fig. B5, Appendix B, and also Salim et al. 2023). The expected relationship between SFR and the star-forming radius is described by the equation:

$$SFR = \frac{A_{KS}}{\pi^{n-1}}\frac{M_{gas}^n(< R_{SF})}{10^{6n}R_{SF}^{2(n-1)}} = \frac{A_{KS}}{\pi^{0.42}}\frac{M_{gas}^{1.42}(< R_{SF})}{10^{8.52}R_{SF}^{0.84}}. \tag{12}$$

Here, we utilized the value of the KS exponent $n = 1.42$ and the term 10^{6n} is related to the fact that sizes are used in units of kpcs. Notice that all the quantities involved in equation (12) depend on stellar mass, particularly emphasizing the relationship with gas mass.

We utilize the data provided by de los Reyes & Kennicutt (2019) from nearby spirals to analyse the gas mass within R_{SF} relative to stellar mass. To ensure consistency with our adopted IMF, we adjust the stellar mass by subtracting 0.24 dex and the SFRs by subtracting 0.05 dex from the values reported by de los Reyes & Kennicutt (2019). They originally employed a Salpeter (1955) IMF using the estimator proposed by Eskew, Zaritsky & Meidt (2012) for stellar mass determination and a Kroupa (2001) IMF with the estimator from Murphy et al. (2011) for SFR estimation. Additionally, we select SFMS galaxies as described in Section 2.3. Fig. 10 shows the strong correlation between $M_{gas}(< R_{SF})$ and M_* for SFMS given by

$$\log\left(\frac{M_{gas}}{M_\odot}\right) = (0.76 \pm 0.03) \times \log\left(\frac{M_*}{M_\odot}\right) + (1.62 \pm 0.27), \tag{13}$$

and with a small dispersion around it of $\sigma_{gas} = 0.29$ dex. Consequently, when fixing the stellar mass, the gas mass remains approximately constant (see also Calette et al. 2018). Additionally, fixing the stellar mass helps eliminate any extra correlation between mass and the SFR and size. In conclusion, we can reasonably assume that equation (12) reduces to SFR $\propto R_{SF}^{-0.84}$ for a given stellar mass. Since our objective is to correlate the SFR with R_e, the next step is to establish a relationship between R_{SF} and R_e.

As discussed in de los Reyes & Kennicutt (2019), R_{SF} is a factor of ≈ 1.83 smaller than the Holmberg (1950) radius in nearby spirals. According to the fit provided by Salim et al. (2023), the Holmberg radius is given by $R_{25} \propto R_e^{0.333} \times M_*^{0.188}$. The above implies that $R_{SF} \propto R_{25}$ and therefore at fixed M_* the KS law, equation (12), gives

$$SFR \propto R_e^{-0.28}. \tag{14}$$

This relation is indeed closer to the ones found in Fig. 4 (cyan dashed lines) and consistent with shallower trends with the half-light radius. Therefore, we conclude that the global KS law is indeed consistent with the relationship between size and SFR described in Section 3.
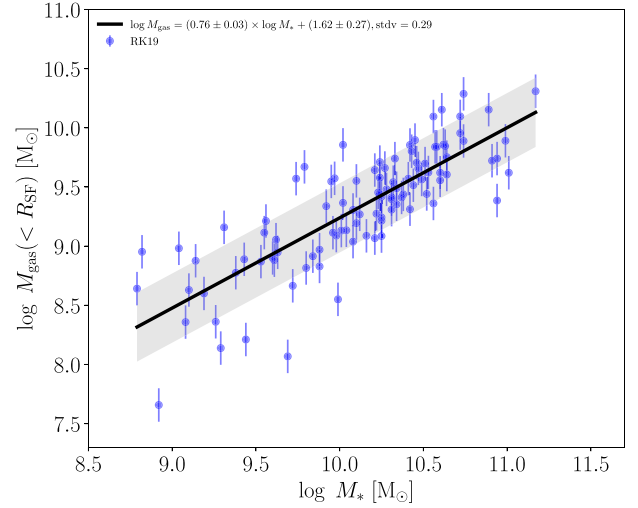
Figure 10. The gas mass within the star-forming radius R_{SF} is shown as a function of stellar mass from de los Reyes & Kennicutt (2019) for SFMS. There is a strong correlation between gas mass and stellar mass, with small dispersion (including random errors) around it ($\sigma_{gas} = 0.29$ dex). This indicates that, for a given stellar mass, the gas mass (within R_{SF}) remains approximately fixed.

Next, we expand further our discussion and we employ the global KS law to calculate gas masses from SFRs and sizes; that is, we will use the inverted global KS law to obtain M_{gas}, to further explore the implications of the global KS law. Due to scatter in the KS law, inverting this relationship involves considering the scatter around the relation. Unfortunately, the literature lacks a comprehensive characterization of the inverted global KS law. To address this, we utilize data from de los Reyes & Kennicutt (2019), who revisited the global KS law for spiral galaxies, and the compilation and homogenization from Calette et al. (in preparation).[9] Based on the information from these two papers, we perform an unweighted linear regression, expressed as

$$\Sigma_{gas} = \alpha_{KS}\Sigma_{SFR}^\eta. \tag{15}$$

The results show $\eta = 0.44 \pm 0.02$ and $\log(\alpha_{KS}/M_\odot\,pc^{-2}) = 2.09 \pm 0.04$ with a dispersion, including random errors, of 0.19 dex. It is important to note that $n \neq 1/\eta$. For further details, refer to Appendix B.

As defined by the global KS law, the gas mass is composed of atomic, H I, and molecular, H$_2$, hydrogen. Molecular clouds, which account for most of the molecular hydrogen in galaxies, are the sites where the star formation occurs. To understand the relationship between SFR, gas mass, and size, it is key to study the fraction of molecular hydrogen in galaxies. Our next step is to derive an empirical correlation between M_{H2}, SFR, and M_* to predict the mass of molecular hydrogen in galaxies (see e.g. Feldmann 2020). Moreover, a study of this relationship has led Dou et al. (2021) to find evidence that the star formation laws observed in both starburst and

---

[9]In our study, we utilize a subsample compiled by Calette et al. (2018), which heavily relies on the xCOLDGASS sample by Saintonge et al. (2017). This subsample is defined in a manner similar to that described in the main body of this paper, selecting SFMS galaxies and requiring detections in both M_{HI} and M_{H2}. It is worth noting that in our forthcoming work, Calette et al. (in preparation), we employ the conversion factor between CO luminosity and H$_2$ mass from Accurso et al. (2017).
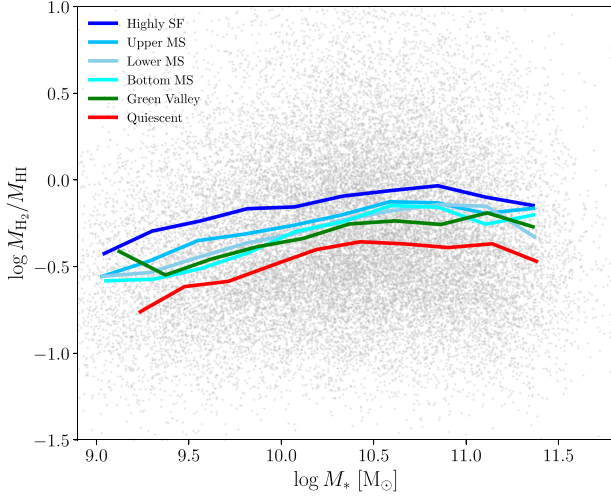
Figure 11. Predicted H$_2$/H I ratios as a function of M_* (see the text and Appendix B for details). The grey dots show the distribution of SDSS central galaxies, while the solid lines show the average H$_2$/H I ratios for each central galaxy subsample of SFMS galaxies (see Table 1). HSF galaxies exhibit larger H$_2$/H I ratios followed by UMS. No clear trends are observed between LMS BMS and GV galaxies, while quiescent galaxies have the lowest ratios.

SFMS galaxies may have similarities to those in quiescent galaxies (see also Tacconi et al. 2018; Tacconi, Genzel & Sternberg 2020, but see Daddi et al. 2010). While we primarily focus on SFMS galaxies in this section, we use the above argument and show some results for quiescent galaxies in Figs 11 and 12, although we do not discuss them in detail. We compute H$_2$ masses by using the following empirical relationship (details can be found in Appendix B),

$$\Sigma_{H_2}(\text{SFR}, M_*) = \alpha_{H_2} \times \Sigma_{SFR}^{0.57 \pm 0.03} \times \Sigma_*^{0.46 \pm 0.05}. \quad (16)$$

Here, $\log(\alpha_{H_2}/M_\odot \text{ pc}^{-2}) = -1.75 \pm 0.47$ with a dispersion, including random errors, of 0.19 dex and as above we define the following surface densities: $\Sigma_{H_2} = M_{H_2}/\pi R_{SF}^2$ and $\Sigma_* = M_*/\pi R_{SF}^2$.

It is interesting to note that adding the two exponents in equation (16) the result is ~ 1. The above has two important consequences:

(i) H$_2$ mass does not depend or depends very weakly on radius. In general, if $\Sigma_{H_2} \propto \Sigma_{SFR}^\alpha \times \Sigma_*^\beta$ and $\alpha + \beta = 1$ then this is equivalent to $M_{H_2} \propto \text{SFR}^\alpha \times M_*^\beta$ such that there is no dependence with R_{SF} (for the exact values from our fits, $M_{H_2} \propto \text{SFR}^{0.57 \pm 0.03} M_*^{0.46 \pm 0.05} \times R_{SF}^2/R_{SF}^{2.06 \pm 0.12}$). In other words, the H$_2$ depletion times, $t_{dep,H_2} \equiv \Sigma_{H_2}/\Sigma_{SFR}$, are independent of radii for SFMS galaxies (Tacconi et al. 2018).

(ii) Dividing by M_* in both sides of the equation, then $M_{H_2}/M_* \propto M_*^{0.03}\text{sSFR}^{0.57}$, that is, the ratio M_{H_2}/M_* depends strongly on the sSFR of the galaxy, consistent with the results obtained by Dou et al. (2021).

So far, we have (i) a way to estimate the gas mass, M_{gas}, of galaxies by means of the inverted global KS law using the SFR, R_e and M_* of galaxies, and (ii) a way to estimate the molecular gas mass, M_{H_2}, by means of equation (16) using the SFR and M_* of galaxies. From both quantities, we can calculate the molecular gas fraction, $f_{H_2} = M_{H_2}/M_{gas}$ or the H$_2$-to-H I mass ratio, $M_{H_2}/M_{HI} = f_{H_2}/(1 - f_{H_2})$. Since depletion times are independent of radii, we anticipate that f_{H2}, and therefore the H$_2$-to-H I ratio, depends mostly on SFR and the size of the star-forming region R_{SF} (which at the same time depends on M_* and R_e, see above and Salim et al. 2023) as shown by the first

equality in the equation below:

$$f_{H_2}(M_*, \text{SFR}, R_e) = \frac{t_{dep,H_2}(M_*, \text{SFR})}{\alpha_{KS}} \Sigma_{SFR}^{1-\eta}$$
$$= \frac{\alpha_{H_2}}{\alpha_{KS}} \frac{\Sigma_{SFR}^{0.59}}{\text{sSFR}^{0.46}}, \quad (17)$$

where we used the definition of the H$_2$ depletion time, equation (16), and the best values obtained for the inverted global KS law.

The predicted M_{gas} and M_{H_2} masses from our models are compared to the measured ones in Fig. B3. The predictions nicely recover the gas and molecular masses, M_{gas} and M_{H_2}, respectively, for the majority of the galaxies with a random dispersion of ~ 0.2 dex.

Once we have constrained the best fit parameter for α_{KS} and η, our attention turns to the SDSS catalogue. Utilizing the inverted KS relation, $\Sigma_{gas} \propto \Sigma_{SFR}^{0.44 \pm 0.02}$ and the molecular relation $\Sigma_{H_2} \propto \Sigma_{SFR}^{0.57 \pm 0.03} \times \Sigma_*^{0.46 \pm 0.05}$ we can deduce M_{gas}, M_{H_2}, and M_{HI} if the SFR, M_* and R_{SF} are known. Notice that M_{gas} and M_{HI} represent the total gas and H I mass enclosed within the radius R_{SF}, which are either lower or equal to their global masses within the entire galaxy. In the case of H$_2$, it represents the total mass. For our purposes, this distinction is sufficient, as our focus is on understanding the impact of the global KS law on the relationship between SFR, gas mass, and size within the star-forming regions.

Fig. 11 shows the H$_2$-to-H I mass ratio predicted by our model as a function of stellar mass for our SDSS sample. The grey dots are individual galaxies and the solid lines are the mean $\langle \log M_{H_2}/M_{HI} \rangle$ ratios as a function of mass for our subsamples defined in Table 1. At all masses, HSF galaxies, on average, exhibit larger M_{H2}/M_{HI} ratios compared to other SF classes. HSF are followed by UMS galaxies while LMS, BMS, and GV galaxies show similar ratios. Quiescent galaxies have the lowest ratios. Recall that M_{HI} has been derived within R_{SF}. In general the trends are weak, differences between HSF and BMS are not larger than a factor of ~ 2, but there are hints that this ratio displays a monotonic behaviour that is expected from the global KS law, that is, HSF galaxies have elevated values of star formation because they have a larger fractions of H$_2$ masses. A better way to see this is in Fig. 12.

Fig. 12 shows the H$_2$-to-H I mass ratio as a function of Δ_{MS} for five different mass bins as shown in the panels. The grey points are the predicted H$_2$-to- H I mass ratios for individual galaxies in our sample, while the red lines show the mean values and the shaded areas are the errors of the mean. The black filled symbols show the observed values from the Calette et al. (in preparation) compilation. If we focus on galaxies in the SFMS, i.e. $\Delta_{MS} > -0.45$, and below $3 \times 10^{10} M_\odot$, we notice that on average the H$_2$-to-H I mass ratio trends are weaker at $-0.45 < \Delta_{MS} < 0$ and increases towards higher SFRs, in particular for HSF galaxies, consistent with Fig. 11. It increases a factor of ~ 2 from $\Delta_{MS} \sim 0$ to $\Delta_{MS} \sim 0.6$ in the first mass bin and ~ 1.5 and ~ 1.4 times in the second and third mass bin, respectively. Above $3 \times 10^{10} M_\odot$, the H$_2$-to-H I mass ratio, on average, remains roughly constant for the fourth and fifth mass bins.

Fig. 13 shows the H$_2$-to-H I mass ratio, predicted by our model as function of half-light radius, R_e, for five different stellar masses. Notice that this figure exclusively displays SFMS galaxies. This is because GV and quiescent galaxies at higher masses exhibit similar or even larger sizes than SFMS galaxies. This exclusion is important to prevent potential misleading conclusions that could arise from flattening trends between the H$_2$-to-H I mass ratio and sizes due to their comparable sizes. Fig. 13 shows that for galaxies with masses lower than $M_* \leq 3 \times 10^{10} M_\odot$, there is a clear and monotonic trend in each panel between R_e and the ratio H$_2$-to-H I mass ratio. This trend
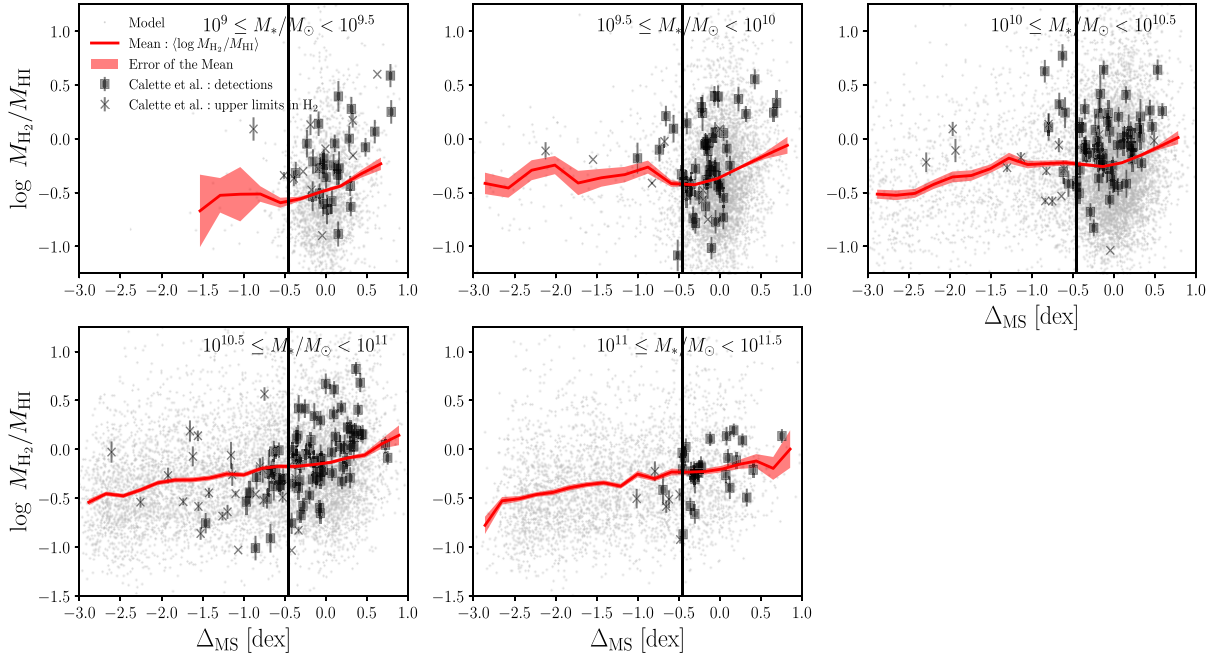
Figure 12. Predicted H_2-to-HI mass ratio from the inverted global KS law and the $\Sigma_{H_2} - \Sigma_{SFR} - \Sigma_*$ relationship as a function of their distance to the SFMS, Δ_{MS}, for five different stellar masses. In each panel, grey dots are individual galaxies while the red solid lines show the mean $\log_{H_2}/M_{HI}$ and the light red shaded are the error this mean. The solid line is the boundary that divides GV from SFMS galaxies. The filled square symbols show observations from the Calette et al. compilation with detections in both H_2 and H I gas masses, while the skeletal symbols are those with upper limits in H_2 masses only. Note the monotonic trend between H_2-to-H I and Δ_{MS} for SFMS. This is more evident for galaxies with masses below $M_* < 10^{10.5} M_{\odot}$.
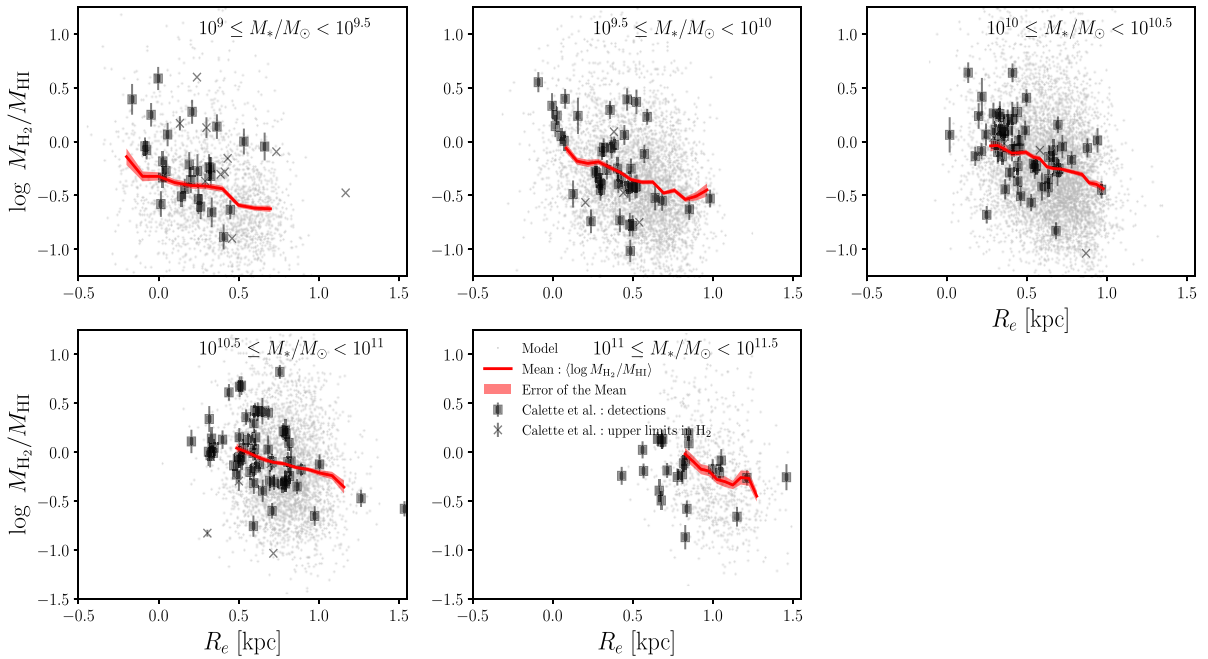
Figure 13. Predicted H_2-to-HI mass ratio and the $\Sigma_{H_2} - \Sigma_{SFR} - \Sigma_*$ relationship as a function of R_e for five different stellar masses and for SFMS only. Similarly to Fig. 12, the solid lines are the mean of the log, the shaded area the error of the mean, and the symbols are from the Calette et al. compilation. On average, there is a negative monotonic trend between the H_2-to-HI mass ratio and R_e. This is a consequence of the fact that in compact galaxies the conversion of HI into H_2 is more efficient.

goes in the direction that at a given stellar mass, those galaxies with higher values of H_2-to-H I mass ratio, and thus larger molecular gas ratios, are more compact. For example, the ratio of smaller galaxies, $R_e \sim 1.6$ kpc, is a factor of ~ 2.7 lower than larger galaxies $R_e \sim 5$ kpc, at masses of $\sim 2 \times 10^9 M_\odot$. At the second and third bins, the differences between the smallest and the largest galaxies are, respectively, a factor of ~ 2 and ~ 1.5. As we approach to higher masses the H_2-to-H I mass ratio, on average, increases by a factor of ~ 1.6 from $R_e \sim 3$ to ~ 10 kpc at the fourth mass bin and by the same amount at fifth bin between $R_e \sim 6$ and ~ 17 kpc. Our findings agree in a general way with those of Lin et al. (2020), who also pointed out higher molecular gas fractions in smaller radii galaxies, though our results differ quantitatively owing to the different scaling laws used.

The trends observed in Figs 11–13 reveal that the H_2-to-H I mass ratio, and thus the fraction of molecular gas, depends more on R_e than on the SFR. This can be understood as follows: if in equation (17), we substitute $R_{SF} \propto R_e^{0.333} M_*^{0.188}$, then $f_{H_2} \propto M_*^{0.24} SFR^{0.13}/R_e^{0.4}$. At fixed stellar mass, galaxies with smaller radii are compact and denser. Notice that

$$f_{H_2} \propto sSFR^{0.13} \mathcal{C}^{0.4}, \tag{18}$$

where $\mathcal{C} = M_*/R_e$ is the compactness (and we omitted a small dependence of $M_*^{0.02}$ in f_{H_2}). In other words, the primary relation is between the fraction of molecular gas and the compactness of the galaxy while the sSFR introduces some scatter around this relation. None the less, we stress that the above is just a consequence of the relationship between the star-forming region with the half-light radius of the galaxy and the physical correlation is with the size of the star-forming region since

$$f_{H_2} \propto SFR^{0.56} R_{SF}^{-1.12}. \tag{19}$$

Finally, if we assume that in SFMS galaxies the star formation is regulated by the local density of the interstellar medium, ISM, and the pressure of the ISM is determined by the density of the gas and stars, then $M_{H_2}/M_{H_I} \propto P^\alpha$ with $\alpha = 0.92$ (Blitz & Rosolowsky 2006). Therefore, in high-pressured galaxies (which correspond to those more compact), the conversion of H I into H_2 is more efficient, which is what equation (17) predicts.

The important results of this section are summarized in Figs 12 and 13. According to the inverted global KS law and the $\Sigma_{H_2} - \Sigma_{SFR} - \Sigma_*$ correlation (equation 16), which predicts the gas and molecular masses, galaxies with higher H_2-to-H I mass ratios correspond mostly to compact galaxies for a given M_* (Fig. 13). On the other hand, the H_2-to-H I mass ratio as a function of the SFMS deviation (Fig. 12) has a monotonic behaviour for galaxies less massive than $\sim 3 \times 10^{10} M_\odot$ and a weaker correlation for more massive galaxies. Therefore, (i) the galaxy radius R_e at a given M_* correlates well with the H_2-to-H I mass ratio, and (ii) its complex interplay with the SFR (or the deviation from the SFMS) is mostly a consequence of the behaviour of the H_2-to-H I mass ratio with the SFR. These results imply that any interplay between SFR and radius for a given M_* is not primary, but a consequence of the more direct interplay between radius (or compactness) and the H_2-to-H I mass ratio (see equation 18); the galaxy compactness seems to be a relevant property for the process of transforming H I into H_2, which is the first step to later form stars.

6 PATHS FOR GALAXY QUENCHING

The results presented in this paper consistently demonstrate a characteristic mass of $M_c = 2 \times 10^{10} M_\odot$ at which the trends in the structural parameters of the galaxies (i.e. morphology) exhibit

a notable change in behaviour across the SFMS. This characteristic mass is close to the observed *bend* of the SFMS as constrained in equation (8), see Fig. 2. For masses below M_c the SFMS follows a power law SFR $\propto M_*^{0.85}$, whereas at higher masses the SFMS flattens out, with SFR$(M_*) \sim$ const. It is noteworthy that M_c aligns with characteristic masses identified in prior studies, albeit somewhat smaller (see also Daddi et al. 2022, for a similar realization). For instance, Kauffmann et al. (2003, see also Bell et al. 2012) identified a characteristic mass of $3 \times 10^{10} M_\odot$ through the analysis of galaxy star formation activity and structural properties. Others have proposed characteristic masses based on analyses of the galaxy stellar mass function or the fraction above which quiescent galaxies represent more than 50 per cent of the population, ranging from approximately $4–8 \times 10^{10} M_\odot$ (see e.g. Bell et al. 2003; Bundy et al. 2006; Drory & Alvarez 2008; Peng et al. 2010; Pozzetti et al. 2010; Baldry et al. 2012; Ilbert et al. 2013; Muzzin et al. 2013). Additionally, the maximum of the stellar-to-halo mass ratio at a given stellar mass is reached around $\sim 3.2 \times 10^{10} M_\odot$ (according to equation 66 from Rodríguez-Puebla et al. 2017) resulting in haloes of $M_{vir} \sim 10^{12} M_\odot$. Note, however, that all these characteristic masses refer to transitions between one population dominating over the other. In our case, we emphasize that M_c refers to a characteristic mass revealing substructure among the relationships between galaxy properties *within* the SFMS. With this distinction in mind, we proceed with our discussion.

Our characteristic mass M_c corresponds to a halo mass of $M_{vir} \sim 10^{11.8} M_\odot$ when considering SFMS galaxies only (see fig. 12 from Kakos et al. 2024, see also Rodríguez-Puebla et al. 2015). This halo mass, is right on the position where a stable virial shock is expected to form through which the cosmological inflowing gas must cross, resulting in the heating of the infalling gas (Dekel & Birnboim 2006). As a result, star formation is expected to be strongly inefficient above this halo mass. The work conducted by Daddi et al. (2022) arrives at a similar conclusion through the analysis of the bend in the SFMS between $0 \lesssim z \lesssim 4$. However, it is important to note that this conclusion does not encapsulate the entire story. Structural properties of galaxies behave differently above this characteristic mass, suggesting the involvement of other factors. Below M_c, HSF galaxies display structural properties similar to the more compact and denser GV galaxies. Above M_c, galaxies at the of the BMS now exhibit similarity to the structural properties of GV galaxies. Therefore, the capacity of galaxies to alter their structure is crucial in understanding the various mechanisms that cause galaxies to deviate from SFMS (see e.g. Rigamonti et al. 2024).

Next, we divide our discussion into low- and high-mass galaxies according to $M_c = 2 \times 10^{10} M_\odot$.

6.1 Low-mass galaxies: two paths for galaxy quenching

Figs 14 and 15 present the distance to mean SFMS, Δ_{MS}, as a function of the half-light radius, R_e across six mass bins for galaxies with masses below M_c. The data is colour coded by the Sérsic index, n_r, and CG, $\nabla_{(g-i)}$, respectively. In both figures, a horizontal black line is drawn at $\Delta_{MS} = -0.45$ dex to separate the GV and quiescent stages from the SFMS. The horizontal dotted lines are $\Delta_{MS} = \pm 0.25$ dex as a representation of the 1σ distribution of the SFMS. Additionally, the blue dashed line represents the expected relationship between half-light radius and SFR from the global KS law: SFR $\propto R_e^{-0.28}$ (see equation 14). We calibrated the zero point of this relationship by fitting to the mean values of Δ_{MS} versus (R_e) (black circles). An important first conclusion drawn from Figs 14 and 15 is that the *size*
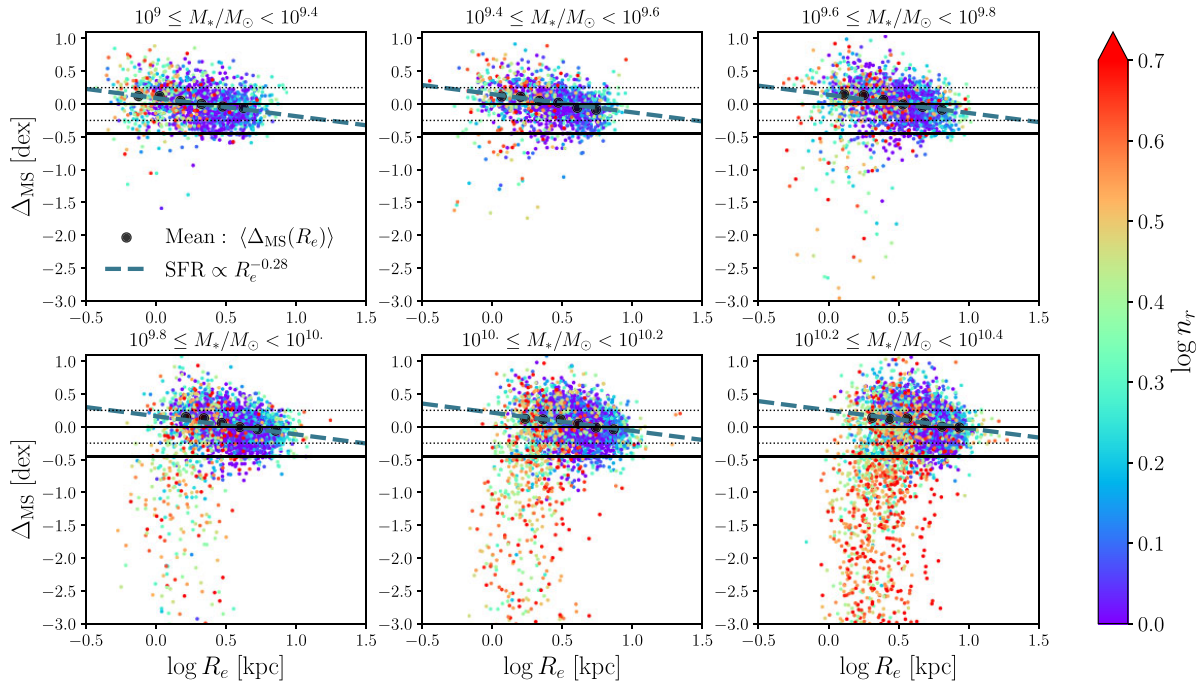
Figure 14. Distance to the main sequence, Δ_{MS}, as a function of the half-light radius colour coded by the Sérsic index for galaxies below $\sim M_c$. The thick horizontal black line at $\Delta_{MS} = -0.45$ dex separates GV and quiescent stages from the SFMS, while the thin and dotted lines are respectively the $\Delta_{MS} = 0$ and $\Delta_{MS} = \pm0.25$. The dashed line shows the expected relationship between size and SFR from the global KS law, SFR$\propto R_e^{-0.28}$, see Section 5. The zero point of this relationship was calibrated using the mean trends of $\Delta_{MS}(R_e)$, black circles. Galaxies positioned above the mean SFMS, particularly those categorized as HSF, tend to exhibit smaller sizes and higher Sérsic indexes, $n_r > 2.5$, similar to those of GV and quiescent galaxies. These galaxies are presumed to quench rapidly by changing undergoing a morphostructural change as an SFMS. These galaxies are expected to maintain their structural parameters, serving as progenitors of quiescent galaxies with higher Sérsic indexes.

of galaxies contributes to the scatter around the SFMS, as observed according to the KS law. It is important to note, however, that the physical correlation is between the *SF radius* with the scatter of SFMS, as discussed in the preceding section.

Figs 14 and 15 synthesize our findings for lower mass galaxies, $M_* \lesssim M_c$. As we *move up* from the mean SFMS, galaxies are smaller and compact, with bluer centres and their light profile becomes more centrally concentrated, and have higher f_{H2} and therefore high H_2-to-H I mass ratios (see Fig. 13). Moreover, galaxies above the SFMS exhibit structural similarities to those in the GV and quiescent galaxies. Particularly, HSF galaxies, see Figs 3–8 and 14. This suggests that HSF galaxies are progenitors of GV galaxies (see also Wuyts et al. 2011, for a similar conclusion). In contrast, as we *descend* from the mean SFMS, galaxies exhibit a structural shift towards being more disc like, $n_r \sim 1$ with redder centres and accompanied by lower H_2-to-H I mass ratios (Fig. 13). This outcome is counterintuitive, as one might expect galaxies at the BMS to be natural candidates for progenitors of GV galaxies, or even quiescent galaxies, as they fade in SF. Our results thus strongly suggest that low-mass galaxies can be quenched through *two distinct processes*, one involving galaxies that will transition above the SFMS, and a second one involving galaxies that will transition at the BMS.

Fig. 16 presents a schematic picture on how SFMS galaxies evolved into GV and quiescent galaxies, assuming that once SFMS galaxies cease their star formation, they do not change significantly their mass and size and Sérsic index (i.e. mass distribution):

(i) Low-mass galaxies above the SFMS as progenitors of GV galaxies: This process involves the production of a centrally con-

centrated mass and a bluer/star-forming centre implying that they undergo a morphostructural change before transitioning out of the SFMS phase. The increase of SFR is due to the observed high H_2-to-H I mass ratios, Fig. 13, most likely in the centre of the galaxy and smaller H_2 depletion times. This transition from the phase of actively forming stars to a more quiescent state is expected to occur relatively quickly in such galaxies. Indeed, as we will show in Fig. 19 galaxies below the SFMS have decreasing SFHs. Mergers, tidal encounters (e.g. Yesuf et al. 2021), or gravitational instabilities (e.g. Cenci et al. 2024) are physical processes that could lead to the enhancement of SFR in the central parts of galaxies and change their morphology, occurring over a time-scale of ~ 70 Myr (Cenci et al. 2024). Additionally, HSF galaxies appear to host a significantly higher number of satellites compared to the average, approximately twice as many within their dark matter haloes (Kakos et al. 2024).

(ii) Low-mass galaxies below the SFMS as progenitors of GV and/or quiescent galaxies: The second process involves the maintenance of a low density in the centre, which results in an old/red centre that characterizes galaxies classified as BMS. This implies an inside–out evolutionary pattern, where the majority of star formation occurs in the outskirts, contributing to the ongoing increase in size. Consequently, the global KS law is expected to respond by decreasing the galaxy's SFR. Additionally, these galaxies are characterized by their low H_2-to-H I mass ratios and larger H_2 depletion times. As shown below in Fig. 19, galaxies at the BMS have nearly constant SFHs over the last ~100 Myr. This is consistent with fact that the transition from the SFMS phase to a quiescent stage should occur over a longer time-scale in these galaxies. In this case, the departure
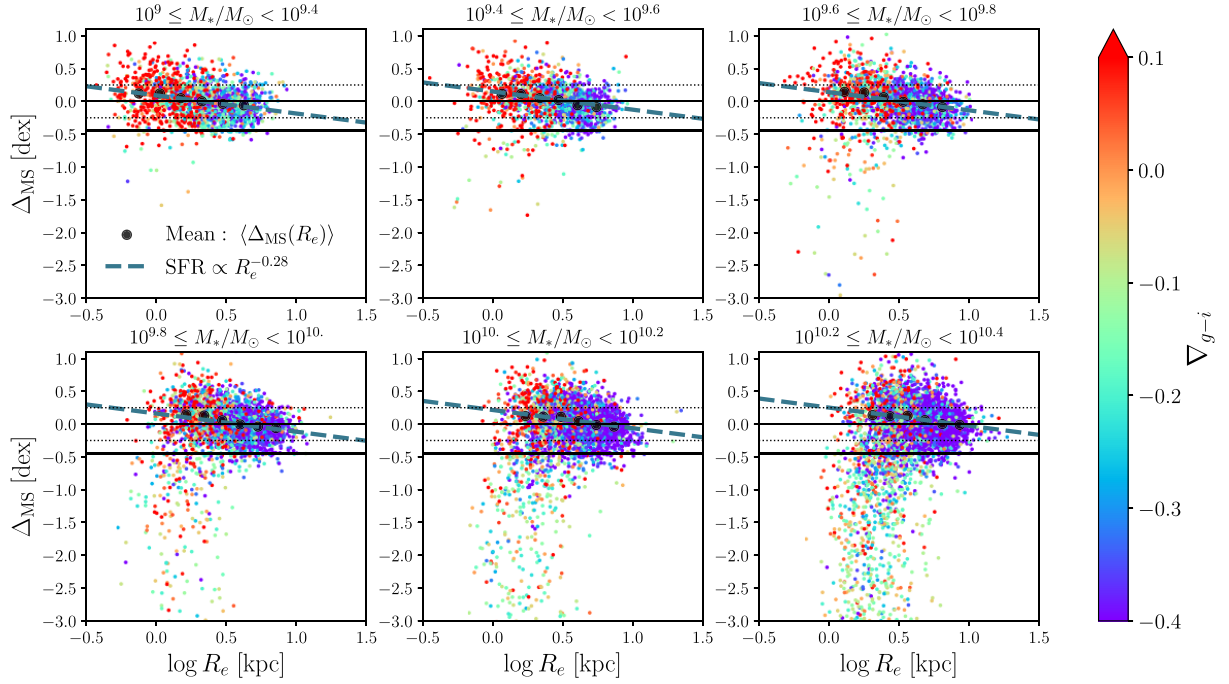
Figure 15. Similar to Fig. 14, we plot the distance to the main sequence, Δ_{MS} as a function of the half-light radius with galaxies colour-coded according to the CG for galaxies below $\sim M_c$. Galaxies above the SFMS tend to exhibit smaller sizes and bluer/star-forming centres, in particular those classified as HSF galaxies. Their sizes, Sérsic indexes (see Fig. 14) and CGs resemble those of the GV and quiescent ones, reinforcing the idea that galaxies above the SFMS are progenitors of the GV and quiescent galaxies. As discussed in the text, these galaxies are expected to quench rapidly by undergoing morphostructural changes as they transition from the SFMS to the GV or to a more quiescent phase (see Fig. 14).

from the SFMS is not related to a morphology change but to a process that does not involve the increase of the central density (see Figs 14 and 15) and also Woo & Ellison (2019). It is unclear how these galaxies will undergo a morphostructural change that matches to those of GV and quiescent galaxies.

Another implication of the above concerns the parallel track hypothesis (van der Wel et al. 2009; van Dokkum et al. 2015; Chen et al. 2020) discussed in the Introduction section. If galaxy size is indeed the next key parameter for galaxy evolution after stellar mass, then our results suggest that the track hypothesis is consistent with our findings. Further studies are needed to fully understand this relationship.

6.2 Higher mass galaxies

Similar to Figs 17 and 18 in the preceding section, we present Δ_{MS} as a function of R_e across six mass bins for galaxies with masses above M_c. It is noteworthy that high-mass galaxies exhibit shallower trends between the SFR and R_e compared to the slope predicted by the KS law, suggesting a deviation from the expected behaviour. Therefore, in contrast to lower masses, the sizes of galaxies do not significantly contribute to the scatter around the SFMS. Additionally, a significant proportion of galaxies above $M_* \sim 3 \times 10^{10} M_\odot$ display higher Sérsic indexes, if those galaxies in the past had lower Sérsic indexes and were within the SFMS, the above indicates structural transformations even within the SFMS (also consistent with Kauffmann et al. 2003; Bell et al. 2012). Notably, the structural parameters of SFMS galaxies are consistent with those of GV and quiescent galaxies. However, a significant difference is observed: *CGs are*

strongly bimodal, with SFMS galaxies exhibiting very negative gradients compared to GV and quiescent galaxies, as shown in Fig. 18. This suggests that while these galaxies are centrally concentrated and may already host a classical bulge, most of their star formation occurs at the outskirts. Surprisingly, this seems sufficient to maintain these galaxies within the SFMS, even when their host dark matter haloes are more massive than the halo mass quenching threshold, $M_{vir} \sim 10^{11.8} M_\odot$. Recently, Hafen et al. (2022) demonstrated the existence of cooling flows with angular momentum, 'rotating cooling flows', that form when gas in haloes is shock-heated to the halo's virial temperature. A key finding in that study is that rotating cooling flows are the primary mode of gas accretion, leading to thin-disc galaxies at $z \sim 0$. While rotating cooling flows can help explain why galaxies have a notable amount of star formation in the outskirts (negative CG), they do not fully elucidate the drastic change in morphology.

In more detail, as we *descend* from the mean SFMS but still remain within the SFMS, galaxies are more compact, dense, with the least red centres and their light profile are more centrally concentrated. Indeed, BMS are structurally closer, none the less still different, to GV galaxies. HSF galaxies, on the other hand, have light profiles that are slightly less centrally concentrated than the BMS and GV galaxies. It is unclear whether HSF galaxies at higher masses represent a stage prior to quenching in the same way that low mass galaxies behave (recall that high mass HSF have more negative CG, redder centre, than their low-mass counterpart (see Fig. 6); i.e. they lack of a younger/bluer centre). We speculate that if HSF galaxies are the progenitors of GV and quiescent galaxies they should evolve different and more slowly than their low-mass counterpart.
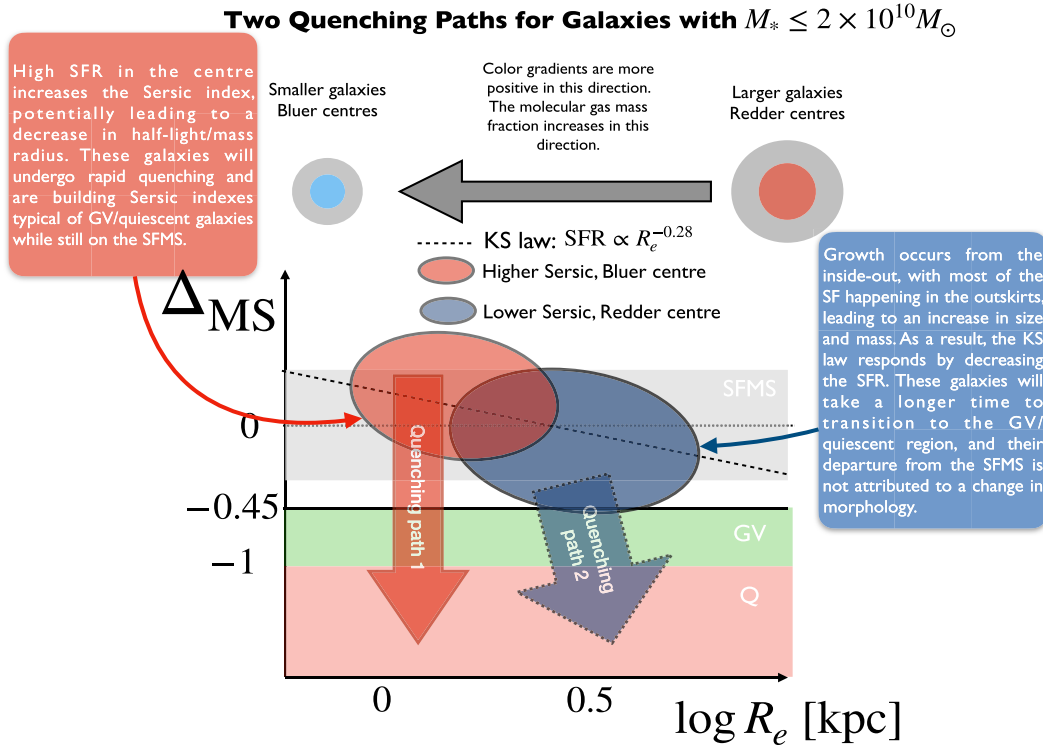
Figure 16. Schematic figure explaining the most important trends observed in Figs 14 and 15. Two paths for galaxy quenching are proposed for galaxies with $M_* \leq 2 \times 10^{10} M_\odot$. **Quenching Path 1:** Galaxies above the mean of the SFMS are smaller and compact, with bluer centres and higher Sérsic indices and H_2-to-H I mass ratios. These galaxies exhibit structural similarities to GV and quiescent galaxies. This suggests that galaxies above the mean of the SFMS, particularly HSF galaxies, are the progenitors of GV and quiescent galaxies. If this is the case, the transition from the SFMS phase should occur quickly in these galaxies, in the direction indicated by the red vertical arrow. Additionally, they undergo a morphostructural change before leaving the SFMS. **Quenching Path 2:** Galaxies below the mean SFMS are larger, with smaller Sérsic indices, redder colours, and lower H_2-to-H I mass ratios. Most of the SF occurs in the outskirts, leading to an increase in their half-light radii and mass. For these galaxies, it will take longer to transition from the SFMS to the GV quiescent region. These galaxies are expected to leave the SFMS, as indicated by the blue arrow with the dotted border. The tilt of the arrow is due to the slow nature of this second path, causing galaxies to gain more mass before transitioning into the GV/quenching region at higher masses. Their departure is not attributed to a change in morphology.

6.3 Further empirical evidence supporting paths for galaxy quenching

In this subsection, we investigate whether additional data supports the pictures described above. In particular, we compare two different kinds of SFRs that can help to understand the most recent SFH of galaxies as a function of their R_e and M_* as detailed below.

Fig. 19 shows the differences between Brinchmann et al. (2004) and Salim et al. (2018) SFRs as a function of M_* for our four different SFMS subsamples[10] (Table 1). In the figure, each galaxy has been colour coded by their distance to $\langle \log R_{e,Q}(M_*) \rangle$ of quiescent galaxies given by

$$\langle \log R_{e,Q} \rangle = \frac{R_{e,0}}{2^{\beta-\alpha}} \left(\frac{M_*}{M_0} \right)^\alpha \left(1 + \frac{M_*}{M_0} \right)^{\beta-\alpha}, \qquad (20)$$

where $\log\left(R_{e,0}/\text{kpc}\right) = 0.18 \pm 0.04$, $\log\left(M_0/\text{M}_\odot\right) = 9.95 \pm 0.08$, $\alpha = -0.01 \pm 0.01$, and $\beta = 0.68 \pm 0.02$.

Brinchmann et al. (2004)[11] modelled the emission lines, including H_α, of SDSS galaxies by means of the Charlot & Longhetti (2001)

[10]We note that a factor of -0.05 dex has been applied to Brinchmann et al. (2004) SFRs to be consistent with a Chabrier (2003) IMF.

[11]The catalogue used in this paper is the updated version that can be found here: https://wwwmpa.mpa-garching.mpg.de/SDSS/DR7/sfrs.html.

model, which combine the Bruzual and Charlot (1997) models with emission line modelling from the code CLOUDY (Ferland 1996). Notice that we are using their global SFRs instead of the results from the fiber. The authors applied the empirical correction described in Salim et al. (2007) by computing the light outside the fibre for each galaxy, and then fit stochastic models, following the colour–colour grid method described by Salim et al. (2007) to this photometry. The authors showed that using the standard Kennicutt (1998a) conversion factor from H_α to SFR is a good average correction for most galaxies. Thus, hereafter we will assume that Brinchmann et al. (2004) SFRs are closely related to H_α SFRs and thus probing time-scales ~ 6–10 Myr (see Calzetti 2013; Flores Velázquez et al. 2021). In the case of Salim et al. (2018), the authors used information from FUV and FIR (see Section 2.3), probing time-scales of ~ 100 Myr (Calzetti 2013; Salim et al. 2016; Salim et al. 2018; Flores Velázquez et al. 2021). Therefore, Fig. 19 shows the difference between two epochs in the SFH of the galaxies. If the difference is negative, the SFR is expected to have faded over the last ~ 100 Myr, while if it is positive, an increase in the SFR is expected for at least towards the last 5–10 Myr. The red solid lines and shaded areas in each panel show the median and the poissonian error.

Fig. 19 supports our previous discussion. Below $M_* \sim M_c (= 2 \times 10^{10} \text{M}_\odot$, vertical shaded area), the median value of the recent SFHs of HSF galaxies have faded by a factor of ~ 1.3 at
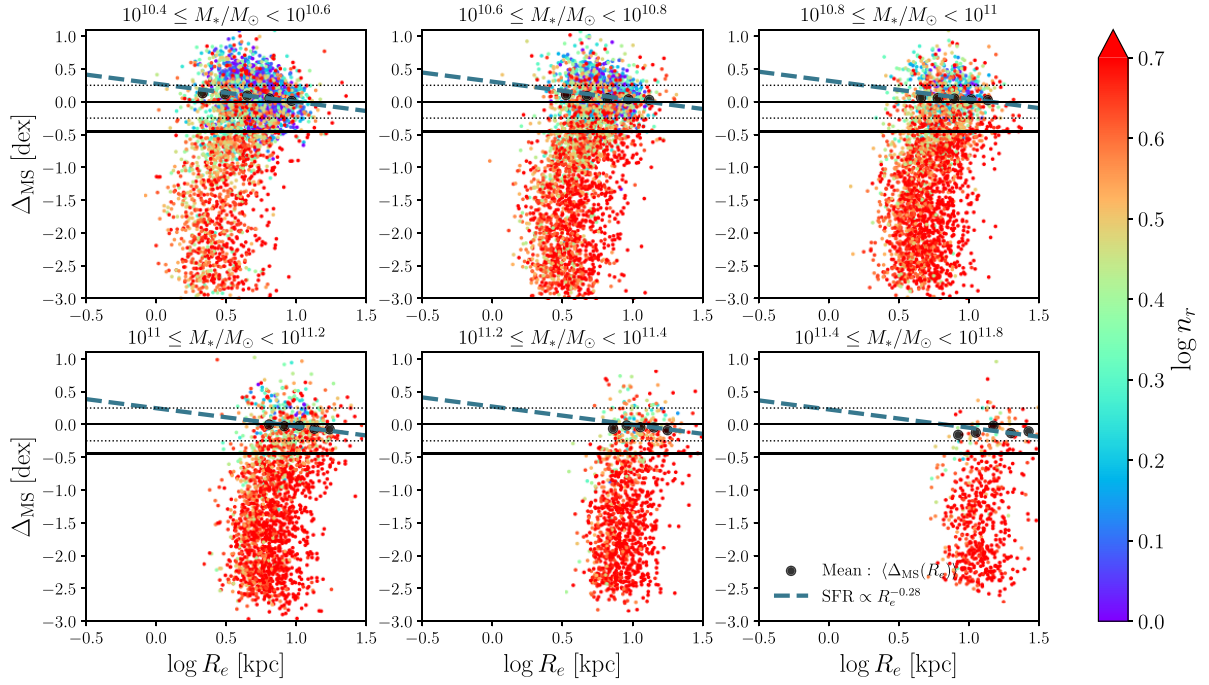
Figure 17. Similar to Fig. 14, the distance to the main sequence, Δ_{MS}, as a function of the half-light radius is shown by colour coding by galaxies Sérsic index for galaxies above $\sim M_c$. High-mass galaxies exhibit shallower trends between the sSFR and R_e compared to the slope predicted by the KS law. Moreover, a significant portion of galaxies above $M_* \sim 3 \times 10^{10} M_\odot$ display higher Sérsic indexes consistent with those of GV and quiescent galaxies. This observation underscores that structural transformations occur even within the SFMS.
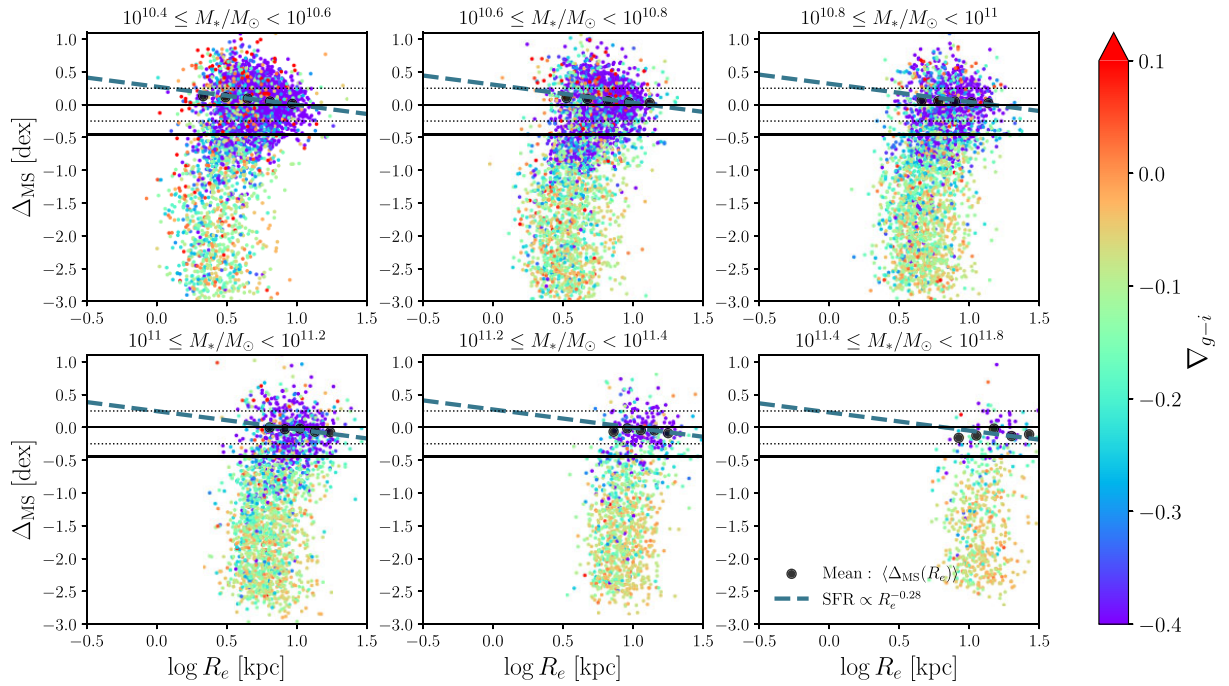
Figure 18. Similar to Fig. 15, we plot the distance to the main sequence, Δ_{MS} as a function of the half-light radius with galaxies colour-coded according to the CG for galaxies above $\sim M_c$. High-mass galaxies not only have higher Sérsic indexes but also very negative CGs indicating that most of the star formation is occurring in the outskirts of these galaxies. Observe how CGs are strongly bimodal.
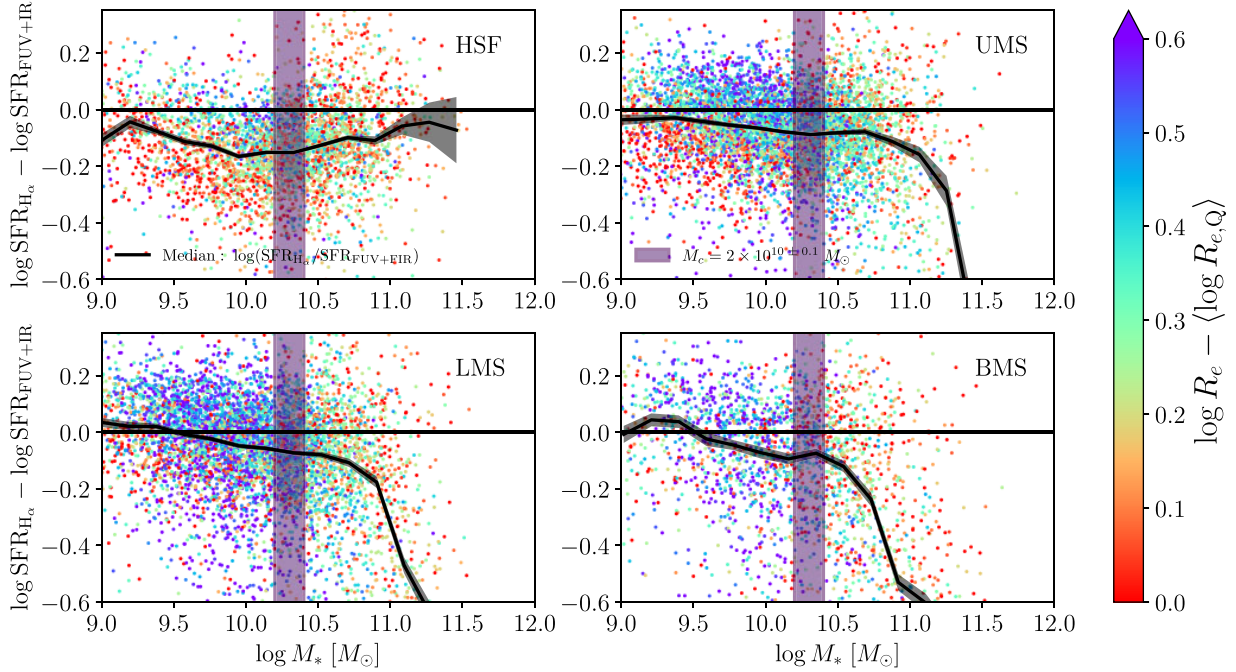
Figure 19. Difference between log SFR determined from H α and FUV + FIR for SFMS, with SFRs from Brinchmann et al. 2004 and Salim et al. 2018, respectively. H α SFRs probe scales between ~ 6 and 10 Myr, while FUV + FIR SFRs probe ~ 100 Myr, representing different points in the SFH of galaxies. Each galaxy is colour coded by their distance to the mean $\langle \log R_{e,Q}(M_*) \rangle$ of quiescent galaxies (see equation 20). Negative differences indicate a decline in recent SFH, while positive differences indicate an increase. When the two are equal, the SFH is constant. The solid red line shows the median relation while the shaded area represents a poissonian error. For masses below M_c, HSF galaxies tend to have decreasing star formation histories, SFHs, at all masses. Similarly, UMS galaxies have decreasing SFHs but to a lesser degree. Galaxies classified as UMS, LMS, and at the bottom of the sequence, BMS, have increasing SFHs at higher masses. AT higher masses than M_c, all the four categories have decreasing SFHs, but notice that the most massive HSF galaxies have closer to constant SFHs.

$M_* \sim 10^9 M_\odot$ and by ~ 1.5 at $M_* \sim 10^{10} M_\odot$ over the last 100 Myr. Furthermore, galaxies with half-light radius comparable to quiescent galaxies have experienced a significant decrease in their recent SFH, fading a median value of ~ 2 at $M_* \sim 10^{10} M_\odot$. Overall, we observe a trend where low-mass HSF galaxies with half-light radii similar to quiescent galaxies are experiencing a decline in their recent SFH, while larger galaxies are closer the zero line. The above results supports the speculation that the transition from active star formation to a quiescent phase occurs rapidly. The median values of UMS galaxies are slightly below the zero line, but once again, we observe a systematic trend: galaxies with half-light radii comparable to quiescent galaxies are experiencing an overall decline in their recent SFHs while larger galaxies are around the zero line. In contrast, the median values of LMS and BMS galaxies are slightly above the zero line (i.e. constant SFH) and slightly below it around $M_* \sim 10^{10} M_\odot$. Overall, their half-light radii are larger compared to quiescent galaxies and their SFHs are approximately constant or even positive. This trend implies that the quenching process from the LMS and BTM to the GV or quiescent may proceed more gradually. Notice that there are some low-mass galaxies in all the panels whose SFHs have decreased substantially, so that, in terms of H α SFRs, these galaxies should be considered GV or even quiescent. Interestingly, at high masses $M_* \gtrsim M_c$, galaxies, on average, have experienced a decline in their SFHs. Specifically, massive UMS, LMS, and BMS galaxies have significantly reduced their SFHs to the extent that some are classified as quiescent galaxies based on the SFR H α estimator. It is worth noting that, despite the decreasing SFHs of the HSF galaxies, they are actually closer to being constant. This

observation might indicate that the transition from actively forming stars to a more quiescent state is faster for SFMS UMS, LMS, and BMS galaxies but slower for HSF galaxies.

Finally, we acknowledge that interpreting Fig. 19 involves some speculation, particularly due to the empirical corrections applied by Brinchmann et al. (2004) based on colours. However, it is encouraging that the figure predicts trends consistent with the discussion at the beginning of this section and previous interpretations, as we will discuss further below. More work needs to be done by using spatially resolved imaging spectroscopy surveys (e.g. Sánchez et al. 2012; Bundy et al. 2015) to make a direct comparison and avoid any aperture correction issues.

7 DISCUSSION

The main goal of this paper was to investigate whether there is a relationship between the distance to the SFMS and the size and morphostructural properties of galaxies. One of the key findings of our study is that there is a non-monotonic relationship between half-light/mass radius and SFR (Figs 3 and 5). This behaviour is also observed in other structural properties, such as the CG (Fig. 6), the central mass density (Fig. 7) and Sérsic index (Fig. 8, see also Figs A3 and A4).[12] However, when analysing trends of the SFR as a function of R_e, we observe a negative monotonic trend, consistent to what one would expect if the SFR were controlled by the KS law (SFR $\propto R_e^{-0.28}$), as depicted in Figs 4, 14, and 15. For

---

[12]This is expected since these other quantities are closely correlated with R_e.

galaxies below $M_c = 2 \times 10^{10}\,\mathrm{M_\odot}$, the SFMS follows a power-law relation, where the SFR scales as SFR $\propto M_*^{0.85}$. Here, M_c is the mass at which the SFMS bends and corresponds to a dark matter halo mass where the formation of virial shocks occurs. Our findings imply that the sizes of galaxies contribute to the scatter around the SFMS. Additionally, we found that the H_2-to-H I mass ratio increases for galaxies above the SFMS (Fig. 12). Our results indicate two quenching paths for low-mass galaxies, $M_* \leq M_c$: one related to a rapid change of morphology, and the other related to a more gradual, secular process (see Fig. 16). At higher masses, $M_* > M_c$, the SFMS flattens out, with SFR(M_*) $\sim$ const., and galaxies appear to undergo structural transformations already within the SFMS.

Next, we compare these results with previous works and discuss on the galaxy–halo connection.

7.1 Comparison with previous works

In this section, we provide a comparative analysis of our findings with recent existing literature on the topic. Recent studies that have investigated the relationship between the structure of the galaxies and sSFR include Wuyts et al. (2011), Brennan et al. (2017), Woo & Ellison (2019), Lin et al. (2020), Walters et al. (2021), and Yesuf et al. (2021).

Wuyts et al. (2011) and Brennan et al. (2017) specifically focused on the relationship between size and sSFR. The results of Wuyts et al. (2011) are similar to ours; these authors found a non-monotonic relation between R_e (also the Sérsic index) and SFR. They also noted that moderate quiescent and highly star-forming galaxies coexist over an order of magnitude in M_*. Although the authors never explicitly specified the validity range of the aforementioned trend, by examining their Fig. 3, it becomes apparent that the trend holds for $M_* \lesssim 10^{10}M_*$. This aligns closely with our findings, where low-mass highly star-forming HSF galaxies exhibit structural similarities to low-mass GV galaxies. In contrast, Brennan et al. (2017) found a monotonic relation between R_e and Δ_{MS}. The authors argued that after carefully eliminating galaxies with poor photometric fits, the trends observed by Wuyts et al. (2011) nearly disappeared. Here, we emphasize that (1) we are using galaxies with good total magnitudes and sizes (Section 2.1), and (2) we had made multiple checks by using other sets of data for galaxy sizes, as discussed at end of Section 3.1, and found the same trends. Therefore, we disagree that by removing galaxies with poor photometric fits the correlation between size and Δ_{MS} disappears.

The recent paper by Lin et al. (2020) also analysed the relationship between size and sSFR for star-forming galaxies on the SFMS only. While their results are generally consistent with ours, they conclude that there was no significant correlation between R_e and sSFR, particularly for galaxies with masses below $\sim 10^{10}\,\mathrm{M_\odot}$. For more massive galaxies, they found a weak correlation and suggested that this could be due to small (more compact) galaxies evolving slowly out of the main sequence. However, Lin et al. (2020) did not emphasize the non-monotonic relationship between R_e and sSFR despite there being some hints in their data (see their fig. 5).

In our interpretation, the non-monotonic relationship indicates two distinct pathways to quenching. Woo & Ellison (2019) investigated the relationship between morphology and quiescence in galaxies and we find that our results are consistent with theirs [note, however, that contrary to Woo & Ellison (2019), our paper deals primarily with SFMS galaxies]. They proposed two different quenching paths, one consistent with the classical 'inside–out' growth, and the other a 'compaction-like' process that feeds the AGN and quenches the

galaxy. Like us, they investigated the Σ_1–M_* relation and found that galaxies on the upper part of this relation tend to have younger centres, and enhanced sSFR, but they also found that they are metal-deficient. Woo & Ellison (2019) suggested that these galaxies most likely go through a compaction-like process triggered by disc and bar instabilities (see e.g. Lin et al. 2017; Chown et al. 2019). These processes can rapidly deplete the available gas, leading to a uniform quenching of the galaxy. They also found that galaxies on the lower part of the Σ_1–M_* relation are consistent with a secular disk growth. These galaxies have low Σ_1 for their M_* have old, metal-rich, and sSFR suppressed in their centres. One of their main conclusions is that age gradient, sSFR, and metallicity depend on the galaxy's position on the Σ_1–M_* relation. These results are consistent with our findings regarding the relationships between SFR and Σ_1, CG, and R_e. Among all these relationships, we find that galaxies with masses below $M_* \sim 10^{10}\mathrm{M_\odot}$ and high SFR also have high Σ_1 and blue centres indicating the presence of younger populations, and their trends are similar to those of GV galaxies, hinting that they migrate relative quickly to the GV. For higher masses, we find a more consistent picture with the gradual 'inside–out' growth and quenching pathway.

The Woo & Ellison (2019) study sheds light on the existence of two quenching paths, including a 'compaction-like' event that is still not fully understood in the local universe (see also Walters et al. 2021; Walters, Woo & Ellison 2022, discussed further below). While we observe galaxies that may be consistent with this path, such as the low-mass HSF galaxies (but less clear for the high mass ones), the underlying mechanisms responsible for these events remain unclear. However, the Yesuf et al. (2021) work on SFMS galaxies provides a possible insight. In Yesuf et al. (2021), the focus was on investigating the structural parameters that predict whether a star-forming galaxy lies above or below the SFMS. Specifically, they found that asymmetry is the most important predictor for the position in the SFR-M_* plane; there is direct relationship between the asymmetry of a galaxy and its SFR. Asymmetry is related to spiral arms and lopsidedness in isolated galaxies, while in mergers or interactions it is related to structural perturbations. Therefore, in our context, it is plausible that HSF galaxies are expected to be more asymmetric compared to the BMS.

Yesuf et al. (2021) suggested two possible mechanisms to explain the correlation between high asymmetry and higher SFR on the SFMS: mergers and tidal encounters that enhance star formation, or enhanced diffuse gas accretion. We notice that the latter could be an efficient mechanism to promote the conversion of H I into H_2. An intriguing finding from Kakos et al. (2024) reveals a higher number of satellite galaxies orbiting around low-mass HSF galaxies. This finding may support the tidal encounter theory proposed by Yesuf et al. (2021). It is still not clear, however, which mechanism dominates the observed correlation. Bottrell et al. (2024) finds that in the TNG50 simulation, mini mergers help to explain the correlation between asymmetry and elevated SFR. Another interesting finding reported by Yesuf et al. (2021) is that a large number of SFMS galaxies with higher asymmetry are bulge-dominated, concentrated and compact, similar to quiescent galaxies. This result is similar to our findings in low-mass HSF galaxies, which tend to have higher Sérsic indices, high Σ_1, and small R_e, except that we find that these galaxies are more similar to GV ones.

It is interesting to note that the study of simulated starburst galaxies by Cenci et al. (2024) from the FIREbox cosmological volume shows that galaxies initiate bursts of star formation in two ways. Below $M_* \sim 10^{10}\mathrm{M_\odot}$, starbursts are often triggered by global gravitational instabilities, while in massive galaxies, tidal torques resulting from

galaxy mergers are responsible for the initiation of star formation bursts. In both cases, the burst of star formation was accompanied by a compaction event and the increase in the fraction of molecular gas, consistent with our results. The above seem consistent with the Yesuf et al. (2021) picture and align with the interpretation of our findings.

Simulations offer an opportunity to better understand the processes that drive the evolution of the central density of star-forming galaxies. Walters et al. (2021) looked at the structural evolution of isolated galaxies in the Illustris TNG100 simulation, specifically at the growth of the central density within 2 kpc, Σ_2, in relation to total stellar mass M_* in galaxies at low z. The authors found that the Illustris TNG100 is able to reproduce the Σ_2–M_* relation, the radial profile of the stellar ages, sSFRs, and metallicities observed in SDSS MaNGA galaxies when comparing to Woo & Ellison (2019). Similar to the results of Woo & Ellison (2019), they found that dense-core galaxies evolve parallel to the Σ_2–M_* relation, whereas galaxies with diffuse cores evolve in shallower trajectories along the Σ_2–M_* relation. Therefore, understanding the core formation in the Illustris TNG simulation was key for Walters et al. (2021). These authors find that sSFR gradients and BH accretion rate are not good predictors of future core growth in the Illustris TNG simulation; they are only indicators of past core growth. Walters et al. (2022) showed that in TNG100 these bluer-centre galaxies quench rapidly.

Disc instabilities have been proposed as being drivers of structural evolution at redshifts $z > 1$ (Dekel & Burkert 2014; Zolotov et al. 2015; Inoue et al. 2016; Avila-Reese et al. 2018; Lapiner et al. 2023), as they cause fragmentation and the inflow of cold gas towards the centre of the galaxy with subsequent bursts of star formation that consume the gas and quench central star formation later. However, Walters et al. (2021) showed that in the TNG simulation, disc instabilities do not lead to core build-up. On the contrary, rapid past core growth results in more stable discs due to the stabilizing effect of spheroids (see e.g. Martig et al. 2009). Interestingly, they find that BH feedback sets a maximum rate of core growth in galaxies with $M_* > 10^{9.5} \, \mathrm{M}_\odot$. This means that in galaxies below that mass, BH feedback does not suppress star formation and rapid core growth. For massive galaxies, they found the total specific angular momentum of gas accretion to be the main predictor of future core growth.

If those TNG galaxies are indeed analogous to ours, these results can help us understand better at least one of the two different quenching paths at low masses. The low-mass, HSF galaxies that we observe have high Σ_1 and bluer centres. One explanation could be that structural evolution triggers the central star formation as the BH feedback would not be sufficiently efficient at these low masses to prevent star formation and therefore a rapid core build-up. However, these galaxies will quickly deplete their gas, and most likely, during that phase, the BH mass will grow enough to quickly transition them into the GV. Another possibility is that strangulation due to gas consumption could take them into the GV or even to quiescent region. In future studies, it will be key to study the occupation of AGNs in HSF galaxies. For masses above $M_* \sim 10^{9.5} \, \mathrm{M}_\odot$, BH feedback prevents future central build-up and allows for a secular (Walters et al. 2021), inside−out quenching; the fossil record analysis of elliptical galaxies from the MaNGA/SDSS-IV survey shows that most of them followed indeed this path (Avila-Reese et al. 2023).

Finally, other previous studies have proposed distinct pathways to explain the quenching of galaxies. Perhaps the closest one among them to ours is Schawinski et al. (2014), who investigated the evolutionary paths of late-type and early-type galaxies through the GV, utilizing morphological information. The authors discovered that these two types of galaxies undergo different mechanisms while transitioning through the GV. In early-type galaxies, quenching is triggered by the rapid depletion of the galaxy's gas reservoir, causing them to briefly stay above the SFMS before experiencing a rapid decline in their SFRs. Conversely, late-type galaxies transition more gradually towards the GV through secular processes. These findings align with our interpretation. However, it is important to note that the authors arrived at these conclusions by studying the GV of *all* galaxies (i.e. they included satellites) and by morphology, rather than central galaxies by their properties according to their distance with respect to the SFMS. In that regard, equating early type to quiescent galaxies might not be appropriate.

7.2 Implications for the galaxy–halo connection

Galaxies formed and evolved within massive dark matter haloes, and it is expected that galaxy properties are linked to the properties of their host haloes. Two halo properties that are thought to regulate SFRs in galaxies are halo accretion and concentration. The former controls the incorporation of gas into the interstellar medium of the galaxy (Avila-Reese & Firmani 2000; Dekel & Mandelker 2014; Rodríguez-Puebla et al. 2016), while the latter is related to the timing of gas infall into the halo, with more concentrated haloes experiencing earlier infall (Avila-Reese, Firmani & Hernández 1998; Wechsler et al. 2002; Gao et al. 2004; Dutton, van den Bosch & Dekel 2010). Additionally, high concentration is expected to lead to more centrally concentrated galaxies and thus smaller sizes (see e.g. Jiang et al. 2019; Liang et al. 2024). Moreover, Lin et al. (2020) suggested that concentrations could potentially control the interplay between SFRs and radii.

Recently, the importance of halo concentration in regulating galaxy size was challenged by Behroozi, Hearin & Moster (2022), who demonstrated, based on environmental information, that halo accretion, which will set the rate of infalling gas, is the primary determinant of galaxy size. Although our paper does not aim to disentangle the relative importance of these properties in controlling both SFRs and galaxy sizes, we note that the non-monotonic relationship between SFR and the effective radius R_e may be embedded in the correlation between these two properties. We caution that if halo accretion and/or concentration dominate SFRs in a monotonic manner (but see Kakos et al. 2024), the same cannot be assumed for R_e or the central density of the galaxy. Rather, it is likely that multiple halo properties (such as the angular momentum of the dark matter halo, λ, which in turn could be related to the angular momentum of the gas) contribute to the regulation of galaxy size and structure (e.g. Dalcanton, Spergel & Summers 1997; Mo, Mao & White 1998; Avila-Reese & Firmani 2000; Firmani & Avila-Reese 2009; Walters et al. 2021; Romeo, Agertz & Renaud 2023; Liang et al. 2024).

8 CONCLUSIONS

In this paper, we made use of 2D photometric Sérsic fits catalogues (Meert et al. 2015, 2016) for galaxies in the SDSS-DR7 to obtain a volume limited sample of galaxies $M_* \approx 10^9 \, \mathrm{M}_\odot$ and with a central resolution at least of ≈ 1 kpc in radius. Our galaxy sample consists of galaxies that have $m_r < 17.77$, $b/a > 0.5$, and a redshift range of $0.005 < z < 0.067$ (Meert et al. 2013, 2015). From the photometric catalogue, we calculated the mass profile, half-mass radius $R_{e,*}$, the average mass density at 1 kpc Σ_1, and the CGs based on their Sérsic parameters for the r, g, and i bands. CGs were obtained by calculating the surface brightness and luminosity profiles with the Sérsic parameters given in the photometric catalogue and then deriving the colour profile. To obtain M_*, we derived five stellar masses and corresponding mass profiles based on five different

mass-to-light ratios and computed the geometric mean of the five determinations, following the methodology described in Rodríguez-Puebla et al. (2020a, see their appendix A, equation 34). In this paper, we focused on central galaxies by using the Yang et al. (2012) catalogue by assuming that the most massive galaxies, in stellar mass terms, are the central ones.

In this study, we separated our sample of galaxies into six subsamples based on their distance from the SFMS relationship, $\Delta_{\mathrm{MS}} = \log \mathrm{SFR} - \langle \log \mathrm{SFR} \rangle$. Our six subsamples were defined as follows: HSF ($\Delta_{\mathrm{MS}} > 0.25$), UMS $0 < \Delta_{\mathrm{MS}} < 0.25$), LMS ($-0.25 < \Delta_{\mathrm{MS}} < 0$), BMS ($-0.45 < \Delta_{\mathrm{MS}} < -0.25$), GV ($-1 < \Delta_{\mathrm{MS}} < -0.45$), and Quiescent (Q, $\Delta_{\mathrm{MS}} < -1$) galaxies. We provide the details of the subsample definitions in Table 1. Our methods were similar to those described in Fang et al. (2018) and Rodríguez-Puebla et al. (2020b). We use the SFRs from Salim et al. (2018).

The main goal of this work was to determine whether a relationship between SFR and galaxy structure exists. In particular, we study whether there is a relationship between SFR and R_e as implied by the Kennicutt-Schmidt law.

Our main results are:

(i) There is a characteristic mass of $M_c = 2 \times 10^{10} \mathrm{M}_\odot$ beyond which the mean of the SFMS bends. At stellar masses below M_c, the SFMS adheres to a power-law relation, where the SFR scales as SFR $\propto M_*^{0.85}$. However, at higher masses, the SFMS flattens out, with SFR(M_*) $\sim$ const..

(ii) When converted to a dark matter halo mass, M_c is consistent with the halo mass scale of $M_{\mathrm{vir}} \sim 10^{11.8}$ where the formation of virial shocks occur (see also Daddi et al. 2022).

(iii) SFMS galaxies exhibit larger radii, both in terms of half-mass and half-light, compared to GV and quiescent galaxies. On average, they possess a lower central mass density (Σ_1) and a lower Sérsic index (n) in comparison to GV and quiescent galaxies. Additionally, SFMS galaxies tend to have more negative CGs ($\nabla_{g-i} < 0$, indicating redder centres) in general. However, we found that the continuous relationship between SFR, size, and structural properties (Σ_1, n and ∇_{g-i}) at a fixed stellar mass is non-monotonic.

(iv) The sizes and structural parameters of the galaxies exhibit a notable change in behaviour across the SFMS at the characteristic mass of $M_c = 2 \times 10^{10} \mathrm{M}_\odot$.

For galaxies below $M_* < M_c$ we found:

(i) Galaxies above the SFMS, in particular, HSF galaxies ($\Delta_{\mathrm{MS}} > \sigma_{\mathrm{MS}}$) typically exhibit the smallest sizes among all SFMS subsamples, considering both half-light and half-mass radii. Regarding their Σ_1, they have the highest central density and tend to have the least negative CGs (bluer centres) compared to other SF subsamples.

(ii) Moreover, lower mass HSF and UMS galaxies exhibit sizes and central densities, Σ_1, that are comparable to those of GV and quiescent galaxies. Given this resemblance, we posit that galaxies above the SFMS might serve as the progenitors for at least a fraction of the GV and quiescent galaxies.

(iii) At masses below $M_* < M_c$, galaxies at the BMS, $-0.45 < \Delta_{\mathrm{MS}} < -\sigma_{\mathrm{MS}}$, exhibit more disc-like characteristics. They have the lowest central density and tend to show negative CGs (indicating redder centres) compared to other SF subsamples. Given that GV and quiescent galaxies are smaller and centrally concentrated with flatter CGs, the above results are counterintuitive, as it is expected that BMS galaxies would be natural candidates for progenitors of GV galaxies and/or quiescent ones.

(iv) Our results strongly suggest that low-mass galaxies ($M_* < M_c$) can undergo quenching through two distinct pathways. The first

pathway involves galaxies above the SFMS, where we speculate that the transition from SFMS to a more quiescent state is relatively rapid. These galaxies experience a morpho-structural change before transitioning out of the SFMS phase. The second pathway involves galaxies with $-0.45 < \Delta_{\mathrm{MS}} < -\sigma_{\mathrm{MS}}$ (BMS galaxies), where the transition from the SFMS phase to a quiescent state might occur over a longer time-scale. In this case, the departure from the SFMS is not related to a change in morphology but to a process that does not involve an increase in central density.

At higher masses ($M_* > M_c$) we found:

(i) BMS galaxies exhibit greater compactness and more centrally concentrated light profiles with the least red centres. Structurally, these massive BMS galaxies are closer to GV galaxies. Conversely, massive HSF galaxies are less centrally concentrated compared to BMS and GV galaxies. In this scenario, BMS galaxies align with the anticipated outcome of being the most likely candidates for progenitors of GV galaxies and/or quiescent ones. However, it is evident that structural transformations are already occurring within the SFMS for high-mass galaxies.

We also studied which among the structural properties is the most relevant in inferring Δ_{MS} by using the Generalised Additive Models (GAM; Hastie & Tibshirani 1990). We found

(i) For low-mass galaxies, ($M_* < M_c$), CGs and Σ_1 are the properties ranked on the top of importance respectively for HSF and UMS. For LMS and BMS R_e was ranked on the top, contrary to previous studies.

(ii) For high-mass galaxies, ($M_* > M_c$), R_e was ranked on the top of importance for HSF and UMS galaxies while for LMS and BMS galaxies, n_r and CGs were ranked on the top, respectively.

Additionally, we developed an empirical model based on the global Kennicutt−Schmidt (KS) law to understand the relation between the SFR and size for a given stellar mass. Our results show that

(i) For galaxies below M_c, the size of galaxies contributes to the scatter around the SFMS in accordance with the KS law. However, at higher masses, the relationship between SFR and size disappears.

(ii) The KS law predicts that the expected relation between SFR and size, for a given stellar mass and assuming a constant gas mass, is SFR $\propto R_e^{-0.28}$. This is consistent with the observed trends from our SDSS sample (see Figs 4, 14, and 15).

(iii) We inverted the global KS law by considering the scatter around this relation and combined it with an empirical model that computes molecular masses from SFRs and M_*. Our analysis reveals that compact galaxies exhibit higher H_2-to-H I mass ratios for a given stellar mass (Fig. 13 and equation 18). Furthermore, we observed a monotonic correlation between H2-to-H I mass ratios and ΔMS. These findings suggest that any interplay between SFR and radius for a given stellar mass is not primary but a consequence of the relationship between radius and H_2-to-H I mass ratios.

Similar to previous studies (e.g. Schawinski et al. 2014; Woo & Ellison 2019; Yesuf et al. 2021), our findings emphasize that quenching is not a straightforward transition of SFMS galaxies evolving through the GV and then ultimately reaching the quiescent region. The evidence presented here suggests that different quenching mechanisms, operating on different time scales, may have influenced the progenitors of GV and quiescent galaxies. This paper marks the beginning of a series that delves into the question of which galaxy properties are the primary predictors for the position relative to the SFMS. In Kakos et al. (2024), we will examine the two-

point correlation function and the stellar-to-halo mass relations as a function of the distance to the SFMS.

DATA AVAILABILITY

The data underlying this article will be shared on reasonable request to the corresponding author.

REFERENCES

Accurso G. et al., 2017, MNRAS, 470, 4750
Avila-Reese V., Firmani C., 2000, RMxAA, 36, 23
Avila-Reese V., Firmani C., Hernández X., 1998, ApJ, 505, 37
Avila-Reese V., González-Samaniego A., Colín P., Ibarra-Medel H., Rodríguez-Puebla A., 2018, ApJ, 854, 152
Avila-Reese V., Ibarra-Medel H., Lacerna I., Rodríguez-Puebla A., Vázquez-Mata J. A., Sánchez S. F., Hernández-Toledo H. M., Cannarozzo C., 2023, MNRAS, 523, 4251
Baldry I. K. et al., 2012, MNRAS, 421, 621
Barro G. et al., 2017, ApJ, 840, 47
Behroozi P., Wechsler R. H., Hearin A. P., Conroy C., 2019, MNRAS, 488, 3143
Behroozi P., Hearin A., Moster B. P., 2022, MNRAS, 509, 2800
Bell E. F., 2008, ApJ, 682, 355
Bell E. F., McIntosh D. H., Katz N., Weinberg M. D., 2003, ApJS, 149, 289
Bell E. F. et al., 2012, ApJ, 753, 167
Bernardi M., Meert A., Sheth R. K., Fischer J.-L., Huertas-Company M., Maraston C., Shankar F., Vikram V., 2017, MNRAS, 467, 2217
Bernardi M., Sheth R. K., Domínguez Sánchez H., Margalef-Bentabol B., Bizyaev D., Lane R. R., 2023, MNRAS, 518, 3494
Blitz L., Rosolowsky E., 2006, ApJ, 650, 933
Bluck A. F. L., Mendel J. T., Ellison S. L., Moreno J., Simard L., Patton D. R., Starkenburg E., 2014, MNRAS, 441, 599
Bottrell C. et al., 2024, MNRAS, 527, 6506
Brennan R. et al., 2017, MNRAS, 465, 619
Brinchmann J., Charlot S., White S. D. M., Tremonti C., Kauffmann G., Heckman T., Brinkmann J., 2004, MNRAS, 351, 1151
Broeils A. H., Rhee M. H., 1997, A&A, 324, 877
Bundy K. et al., 2006, ApJ, 651, 120
Bundy K. et al., 2015, ApJ, 798, 7
Calette A. R., Avila-Reese V., Rodríguez-Puebla A., Hernández-Toledo H., Papastergis E., 2018, RMxAA, 54, 443
Calette A. R., Avila-Reese V., Rodríguez-Puebla A., Lagos C. d. P., Catinella B., 2021, MNRAS, 505, 304
Calzetti D., 2013, in Falcón-Barroso J., Knapen J. H., eds, Secular Evolution of Galaxies. Cambridge Univ. Press, Cambridge, UK, p. 419
Capaccioli M., 1989, in Corwin H. G. J., Bottinelli L., eds, IN: The World of Galaxies. Springer-Verlag, New York, p. 208
Cappellari M., 2016, ARA&A, 54, 597
Caruana R., Lou Y., Gehrke J., Koch P., Sturm M., Elhadad N., 2015, Proceedings of the 21th ACM SIGKDD International Conference on Knowledge Discovery and Data Mining. KDD'15. Association for Computing Machinery, New York, NY, USA, p. 1721
Cenci E., Feldmann R., Gensior J., Moreno J., Bassini L., Bernardini M., 2024, MNRAS, 527, 7871
Chabrier G., 2003, PASP, 115, 763
Charlot S., Longhetti M., 2001, MNRAS, 323, 887
Chen Z. et al., 2020, ApJ, 897, 102
Cheung E. et al., 2012, ApJ, 760, 131
Chown R. et al., 2019, MNRAS, 484, 5192
Conroy C., Dutton A. A., Graves G. J., Mendel J. T., van Dokkum P. G., 2013, ApJ, 776, L26
Daddi E. et al., 2007, ApJ, 670, 156
Daddi E. et al., 2010, ApJ, 714, L118
Daddi E. et al., 2022, A&A, 661, L7
Dalcanton J. J., Spergel D. N., Summers F. J., 1997, ApJ, 482, 659
Dekel A., Birnboim Y., 2006, MNRAS, 368, 2
Dekel A., Burkert A., 2014, MNRAS, 438, 1870
Dekel A., Mandelker N., 2014, MNRAS, 444, 2071
Dou J. et al., 2021, ApJ, 907, 114
Drory N., Alvarez M., 2008, ApJ, 680, 41
Dutton A. A., van den Bosch F. C., Dekel A., 2010, MNRAS, 405, 1690
Elbaz D. et al., 2007, A&A, 468, 33
Elbaz D. et al., 2011, A&A, 533, A119
Eskew M., Zaritsky D., Meidt S., 2012, AJ, 143, 139
Fang J. J., Faber S. M., Koo D. C., Dekel A., 2013, ApJ, 776, 63
Fang J. J. et al., 2018, ApJ, 858, 100
Feldmann R., 2020, Commun. Phys., 3, 226
Ferland G. J., 1996, Hazy, A Brief Introduction to Cloudy 90
Firmani C., Avila-Reese V., 2009, MNRAS, 396, 1675
Flores Velázquez J. A. et al., 2021, MNRAS, 501, 4812
Gao L., White S. D. M., Jenkins A., Stoehr F., Springel V., 2004, MNRAS, 355, 819
Gonzalez-Perez V., Castander F. J., Kauffmann G., 2011, MNRAS, 411, 1151
Hafen Z. et al., 2022, MNRAS, 514, 5056
Hastie T., Tibshirani R., 1990, Generalized Additive Models. Wiley Online Library
Holmberg E., 1950, Meddelanden fran Lunds Astronomiska Observatorium Serie II, 128, 5
Ilbert O. et al., 2013, A&A, 556, A55
Inoue S., Dekel A., Mandelker N., Ceverino D., Bournaud F., Primack J., 2016, MNRAS, 456, 2052
Jiang F. et al., 2019, MNRAS, 488, 4801
Kakos J., Rodriguez-Puebla A., Primack J. R., Faber S. M., Koo D. C., Behroozi P., Avila-Reese V., 2024, preprint (arXiv:2403.01393)
Kauffmann G. et al., 2003, MNRAS, 341, 54
Kauffmann G. et al., 2012, MNRAS, 422, 997
Kawinwanichakij L. et al., 2021, ApJ, 921, 38
Kennicutt R. C. J., 1998a, ARA&A, 36, 189
Kennicutt R. C. J., 1998b, ApJ, 498, 541
Kennicutt R. C. J., De Los Reyes M. A. C., 2021, ApJ, 908, 61
Kennicutt R. C., Evans N. J., 2012, ARA&A, 50, 531
Krajnović D., Cappellari M., McDermid R. M., 2018, MNRAS, 473, 5237
Kroupa P., 2001, MNRAS, 322, 231
Lange R. et al., 2015, MNRAS, 447, 2603
Lapiner S. et al., 2023, MNRAS, 522, 4515
Lee N. et al., 2015, ApJ, 801, 80
Leja J. et al., 2022, ApJ, 936, 165
Leslie S. K. et al., 2020, ApJ, 899, 58
Liang J., Jiang F., Mo H., Benson A., Dekel A., Tavron N., Hopkins P. F., Ho L. C., 2024, preprint (arXiv:2403.14749)
Lilly S. J., Carollo C. M., 2016, ApJ, 833, 1
Lin L., Li C., He Y., Xiao T., Wang E., 2017, ApJ, 838, 105
Lin L. et al., 2020, ApJ, 899, 93
Lou Y., Caruana R., Gehrke J., Hooker G., 2013, in Proceedings of the 19th ACM SIGKDD International Conference on Knowledge Discovery and Data Mining. KDD'13. Association for Computing Machinery, New York, NY, USA, p. 623
Luo Y. et al., 2020, MNRAS, 493, 1686
Martig M., Bournaud F., Teyssier R., Dekel A., 2009, ApJ, 707, 250
Meert A., Vikram V., Bernardi M., 2013, MNRAS, 433, 1344
Meert A., Vikram V., Bernardi M., 2015, MNRAS, 446, 3943
Meert A., Vikram V., Bernardi M., 2016, MNRAS, 455, 2440
Mo H. J., Mao S., White S. D. M., 1998, MNRAS, 295, 319
Murphy E. J. et al., 2011, ApJ, 737, 67
Muzzin A. et al., 2013, ApJ, 777, 18

Noeske K. G. et al., 2007, ApJ, 660, L43

Nori H., Jenkins S., Koch P., Caruana R., 2019, preprint (arXiv:1909.09223)

Omand C. M. B., Balogh M. L., Poggianti B. M., 2014, MNRAS, 440, 843

Pan Z., Li J., Lin W., Wang J., Fan L., Kong X., 2015, ApJ, 804, L42

Park C., Choi Y.-Y., 2005, ApJ, 635, L29

Peeples M. S., Shankar F., 2011, MNRAS, 417, 2962

Peng Y.-j. et al., 2010, ApJ, 721, 193

Pozzetti L. et al., 2010, A&A, 523, A13

Rigamonti F., Cortese L., Bollati F., Covino S., Dotti M., Fraser-McKelvie A., Haardt F., 2024, A&A, 686, A98

Rodríguez-Puebla A., Avila-Reese V., Yang X., Foucaud S., Drory N., Jing Y. P., 2015, ApJ, 799, 130

Rodríguez-Puebla A., Primack J. R., Behroozi P., Faber S. M., 2016, MNRAS, 455, 2592

Rodríguez-Puebla A., Primack J. R., Avila-Reese V., Faber S. M., 2017, MNRAS, 470, 651

Rodríguez-Puebla A., Calette A. R., Avila-Reese V., Rodriguez-Gomez V., Huertas-Company M., 2020a, PASA, 37, e024

Rodríguez-Puebla A., Avila-Reese V., Cano-Díaz M., Faber S. M., Primack J. R., Franco J., Aretxaga I., Santiago-Mayoral E., 2020b, ApJ, 905, 171

Romeo A. B., Agertz O., Renaud F., 2023, MNRAS, 518, 1002

Saintonge A. et al., 2017, ApJS, 233, 22

Salim S. et al., 2007, ApJS, 173, 267

Salim S. et al., 2016, ApJS, 227, 2

Salim S., Boquien M., Lee J. C., 2018, ApJ, 859, 11

Salim S., Tacchella S., Osborne C., Faber S. M., Lee J. C., Ellison S. L., 2023, ApJ, 958, 183

Salpeter E. E., 1955, ApJ, 121, 161

Sánchez S. F. et al., 2012, A&A, 538, A8

Schawinski K. et al., 2014, MNRAS, 440, 889

Schmidt M., 1959, ApJ, 129, 243

Schreiber C. et al., 2015, A&A, 575, A74

Sérsic J. L., 1963, Boletin de la Asociacion Argentina de Astronomia La Plata Argentina, 6, 41

Shen S., Mo H. J., White S. D. M., Blanton M. R., Kauffmann G., Voges W., Brinkmann J., Csabai I., 2003, MNRAS, 343, 978

Simard L., Mendel J. T., Patton D. R., Ellison S. L., McConnachie A. W., 2011, ApJS, 196, 11

Speagle J. S., Steinhardt C. L., Capak P. L., Silverman J. D., 2014, ApJS, 214, 15

Tacchella S., Dekel A., Carollo C. M., Ceverino D., DeGraf C., Lapiner S., Mandelker N., Primack Joel R., 2016, MNRAS, 457, 2790

Tacconi L. J. et al., 2018, ApJ, 853, 179

Tacconi L. J., Genzel R., Sternberg A., 2020, ARA&A, 58, 157

Tortora C., Napolitano N. R., Cardone V. F., Capaccioli M., Jetzer P., Molinaro R., 2010, MNRAS, 407, 144

Walters D., Woo J., Ellison S. L., Hani M. H., 2021, MNRAS, 504, 1677

Walters D., Woo J., Ellison S. L., 2022, MNRAS, 511, 6126

Wang J., Koribalski B. S., Serra P., van der Hulst T., Roychowdhury S., Kamphuis P., Chengalur J. N., 2016, MNRAS, 460, 2143

Wechsler R. H., Tinker J. L., 2018, ARA&A, 56, 435

Wechsler R. H., Bullock J. S., Primack J. R., Kravtsov A. V., Dekel A., 2002, ApJ, 568, 52

Whitaker K. E., van Dokkum P. G., Brammer G., Franx M., 2012, ApJ, 754, L29

Whitaker K. E. et al., 2014, ApJ, 795, 104

Whitaker K. E. et al., 2017, ApJ, 838, 19

Woo J., Ellison S. L., 2019, MNRAS, 487, 1927

Wuyts S. et al., 2011, ApJ, 742, 96

Yang X., Mo H. J., van den Bosch F. C., Pasquali A., Li C., Barden M., 2007, ApJ, 671, 153

Yang X., Mo H. J., van den Bosch F. C., Zhang Y., Han J., 2012, ApJ, 752, 41

Yesuf H. M., Ho L. C., Faber S. M., 2021, ApJ, 923, 205

Zolotov A. et al., 2015, MNRAS, 450, 2327

de los Reyes M. A. C., Kennicutt R. C. J., 2019, ApJ, 872, 16

van Dokkum P. G. et al., 2015, ApJ, 813, 23

van den Bosch R. C. E., 2016, ApJ, 831, 134

van den Bosch F. C., Aquino D., Yang X., Mo H. J., Pasquali A., McIntosh D. H., Weinmann S. M., Kang X., 2008, MNRAS, 387, 79

van der Wel A., Bell E. F., van den Bosch F. C., Gallazzi A., Rix H.-W., 2009, ApJ, 698, 1232

van der Wel A. et al., 2014, ApJ, 788, 28

APPENDIX A: 1D SHAPE FUNCTIONS AND PREDICTIONS

In Section 4, we presented an analysis made by exploiting EBM to support the findings described in Section 3. By training each model for the SF galaxies above the SFMS (i.e. UMS and HSF) and below (i.e. of LMS and BMS, see Section 2.3 and Table 1), each subsample split further into two stellar mass bins, i.e. $9 \leq \log(M_*/M_\odot) < 10.3$ and $\log(M_*/M_\odot) \geq 10.3$, we obtained the relative importance that single features have in inferring the distance from the Main Sequence of galaxies, Δ_{MS}. Fig. 9 shows for the aforementioned galaxy subsamples in the two stellar mass bins the rankings of importance of the features obtained by computing the absolute mean scores in the 1D shape functions. In Figs A1–A4, we illustrate for each subset the correlation matrix among all the features, also including Δ_{MS}, and the 1D shape functions. In this analysis, the use of the correlation matrix is a tool that may provide a general overview of how different quantities are correlated with each other. However, particularly in cases of not strictly linear correlations, the correlation coefficient does not provide any information on how the variation of a given property changes with distance from the MS. Instead, this is the added value that shape functions have in providing a quantitative measure to fixed value of each property.

The aim of the application of EBM, in the case presented in this manuscript, is not to train a set of models on our sample and make predictions on other galaxy samples, but to exploit the high intelligibility of the method to confirm the results presented in Section 3. However, by the very nature of the method, each GAM has been trained on a *training sample* (80 per cent of each galaxy subsample), and tested on a *test sample* (the remaining 20 per cent of each subset). We provide here two metrics to quantify the goodness of the fit: the root mean squared error RMSE, and the coefficient of determination R^2. The RMSE provides a measurement of how predicted values differ from the observed values:

$$\text{RMSE} = \sqrt{\frac{1}{N} \sum_{i=1}^{N} (\mathcal{T}_i - \mathcal{P}_i)^2}, \tag{A1}$$

where $\mathcal{T}_i$ and $\mathcal{P}_i$ are the true (or observed) and predicted values for the ith object, respectively, while N is the size of the sample, in this case, the test sample. Specifically, the closer to 0, the lower the discrepancy. Concerning R^2, this value informs us about the dispersion of the data and the goodness of the model:

$$R^2 = 1 - \frac{\sum_{i=1}^{N} (\mathcal{T}_i - \mathcal{P}_i)^2}{\sum_{i=1}^{N} (\mathcal{T}_i - \bar{\mathcal{T}})^2}, \tag{A2}$$

where $\bar{\mathcal{T}}$ is the mean of all the $\mathcal{T}_i$ with $i = \{1, ..., N\}$. In this case, the closer to 1, the better the model describes the data set. Hence, the RMSE provides a measurement of how the true and the predicted values differ, while R^2 gives an estimate of how the features comprehensively explain the variation in the predicted quantity.

The upper-right panels of Figs A1–A4 show the residual histograms between the nominal Δ_{MS} values in the test samples and their values predicted by the model. In each plot, together with the size of the corresponding test sample, the RMSE and R^2 values are reported. In the case of the HSF and UMS galaxies, we found for both stellar
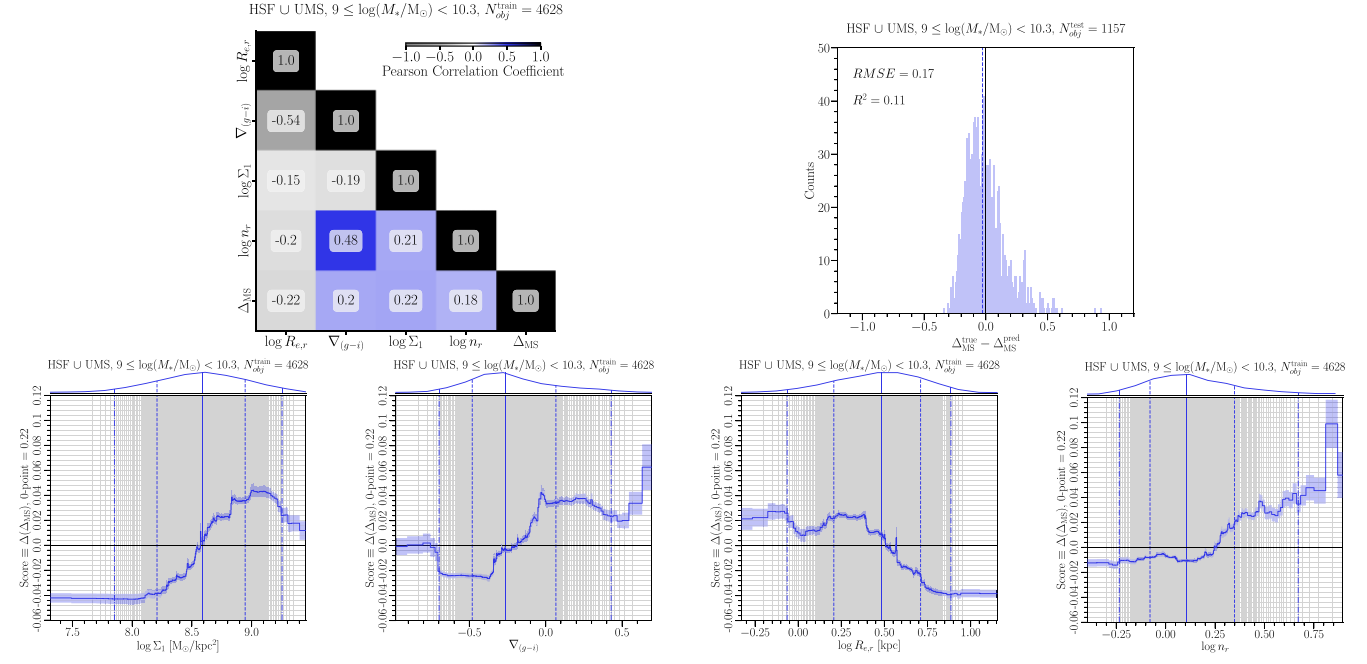
Figure A1. Correlation matrix of the training sample (upper left panel), residual distribution between the predicted and actual values of Δ_{MS} for the test sample (upper right panel), and 1D shape functions (lower panels) sorted for importance (from the left to the right) for HSF and UMS galaxies (i.e. SF galaxies above the SFMS) with $9 \leq \log(M_*/M_\odot) < 10.3$. The correlation matrix cells are coloured as a function of the Pearson Correlation Coefficient of each pair of features and report its value (rounded up to two decimal digits). For each 1D shape function of $\log \Sigma_1$, $\nabla_{(g-i)}$, $\log R_e$, and $\log n_r$, we highlight the median (vertical thick solid line), and the limits for the 68 per cent (vertical thick dashed lines), and 95 per cent (vertical thick dash-dotted lines) ranges of the distribution, the latter displayed on the top of each panel. The vertical grey thin lines mark the edges of the equal-density bins used to evaluate the 1D shape functions. For all the 1D shape functions, the shaded region represents the pseudo-errors from the bagging procedure. The horizontal black thick line tracing the score equal to 0 corresponds to the mean distance from the MS, Δ_{MS}, that is $\simeq 0.22$ dex. The y-axis range is shared among all the plots to facilitate the comparison of the relative contribution of each feature. The residual distribution plot reports the values of RMSE and R^2. The vertical solid line corresponds to 0, while the coloured dashed line is tracing the median of the distribution.
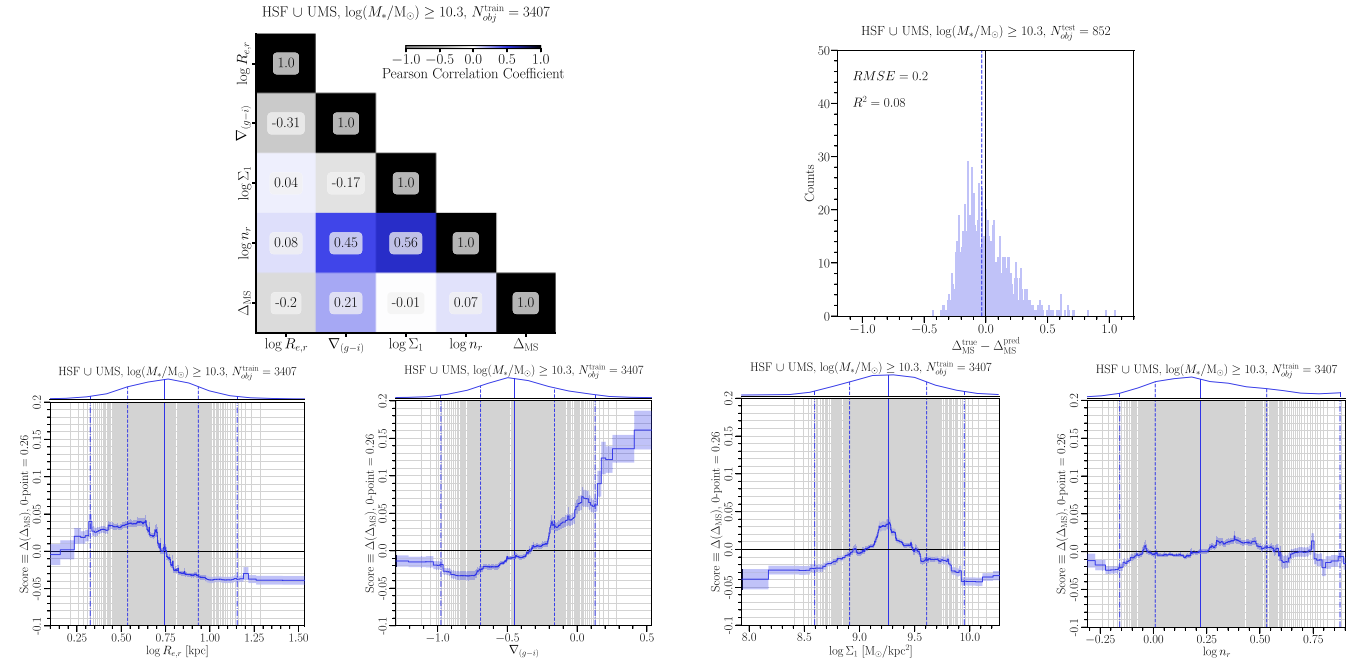
Figure A2. Same as Fig. A1, but for HSF and UMS galaxies (i.e. SF galaxies above the SFMS) with $\log(M_*/M_\odot) \geq 10.3$. The score equal to 0 corresponds to $\simeq 0.26$ dex.
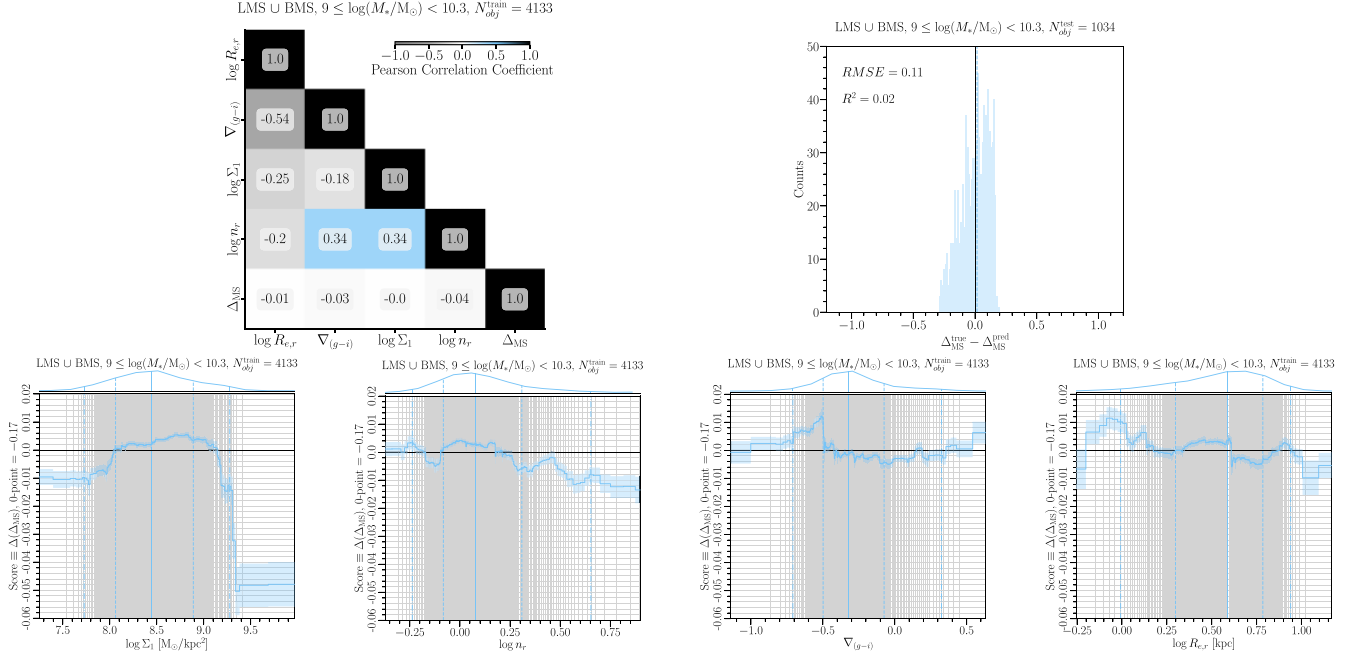
Figure A3. Same as Fig. A1, but for LMS and BMS galaxies (i.e. SF galaxies below the SFMS) with $9 \leq \log(M_*/M_\odot) < 10.3$. The score equal to 0 corresponds to $\simeq -0.17\,\mathrm{dex}$.
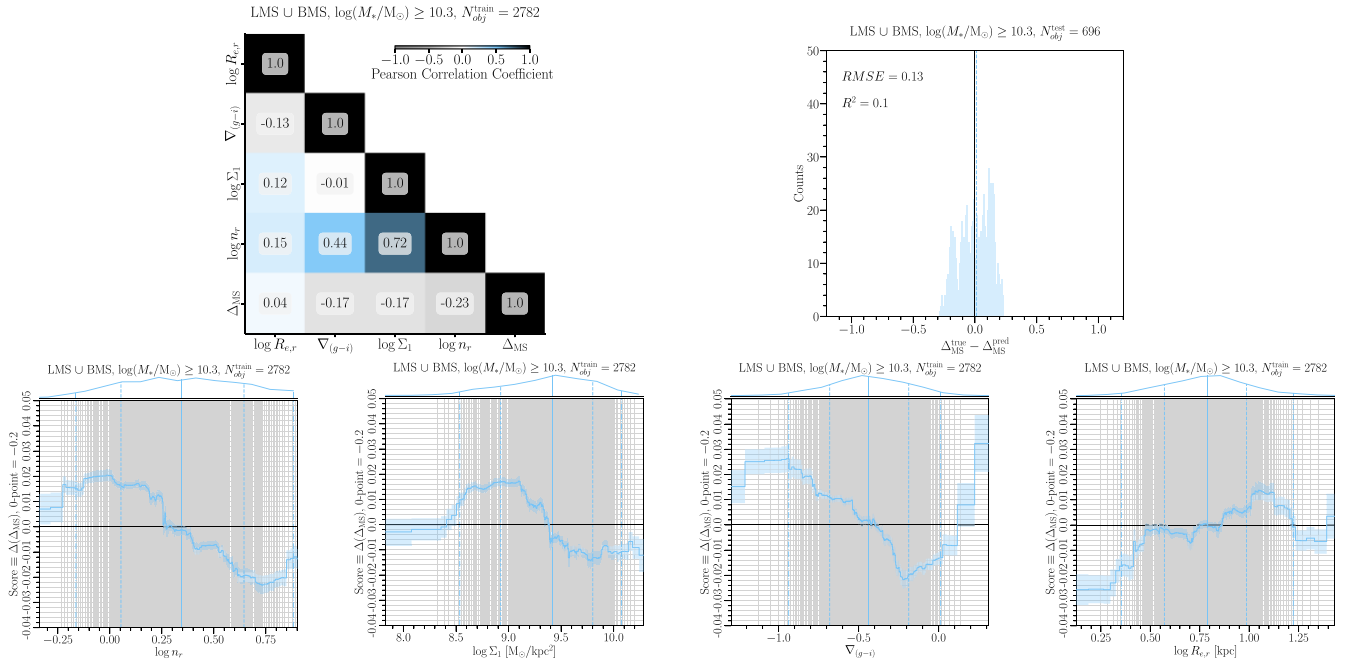
Figure A4. Same as Fig. A1, but for LMS and BMS galaxies (i.e. SF galaxies below the SFMS) with $\log(M_*/M_\odot) \geq 10.3$. The score equal to 0 corresponds to $\simeq -0.2\,\mathrm{dex}$.

mass bins, two Gaussian-like distributions, slightly skewed towards the predicted values. The RMSE are ~ 0.2, while the $R^2 \sim 0.1$. For the LMS and BMS systems, instead, the RMSE reduces to ~ 0.1 and the R^2 is around 0.02 at $9 \leq \log(M_*/M_\odot) < 10.3$, and lightly improved in the high-mass tail, with a value of ~ 0.1. These last two distributions, however, do not resemble a Gaussian and are more noisy than the previous two. A possible explanation for the low R^2 values for the four subsets can be found in the nature of the galaxies samples and their large scatter with respect to the Δ_{MS}.

In conclusion, we stress here again that the scope of applying EBM was to give support to the results presented in Section 3 thanks to the high information level of the method. Indeed, the 1D shape functions presented in Figs A1–A4 confirm all the previous findings, in particular when we focus on the regions containing 68 per cent of each subsample (delimited by dashed lines).

APPENDIX B: THE INVERTED GLOBAL KS LAW AND NEW FITS FOR MOLECULAR HYDROGEN MASSES

In this section, we provide a detailed description of our fits to the inverted Kennicutt–Schmidt (KS) law model and equation (16). To accomplish this, we utilize two samples. The first sample is based on the compilation by Callete et al. (in preparation), heavily relying on the xCOLDGASS sample (Saintonge et al. 2017). In Callete et al., we chose to apply the conversion factor between CO luminosity and H_2 masses proposed by Accurso et al. (2017). Additionally, we cross-matched the Callete et al. sample with those from Meert et al. (2015, 2016) to obtain 2D photometric Sérsic fits for the g, r, and i bands. The second sample is described by de los Reyes & Kennicutt (2019), who recently revisited the global KS law for spiral galaxies. We corrected their H_2 masses to be consistent with the Accurso et al. (2017) correction factors and changed their IMF to ours for consistency.

Our strategy for constraining the best-fitting models for the inverted global KS law and equation (16) is as follows: we utilize the compilation by Callete et al. and estimate Σ_{HI} and Σ_{H_2} such that the relation Σ_{gas} as a function of Σ_{SFR} aligns with the measurements from de los Reyes & Kennicutt (2019). Subsequently, we fit the resulting inverted global KS law using only the Callete et al. sample. We chose the Callete et al. sample over the de los Reyes & Kennicutt (2019) sample because the latter requires additional homogenization efforts with our data (e.g. photometry, morphology, etc.), which goes beyond the scope of this paper. Furthermore, the Callete et al. sample is already consistent with the stellar masses, SFRs, and half-light radius in our SDSS catalogue. Below, we provide a more detailed description of additional calculations performed for the Callete et al. sample.

As outlined in the main manuscript, the global KS law is typically derived by computing the gas mass and SFR within a star-forming region with a radius that encloses approximately 95 per cent of the $H\alpha$ flux of the galaxy. This radius is denoted as R_{SF}. According to de los Reyes & Kennicutt (2019), this star-forming radius is smaller than the Holmberg (1950) radius (R_{25}, the B band 25 mag arcsec^{-2} isophote). Specifically, $R_{SF} = R_{25}/1.83$. To adhere closely to this definition, we employ the model by Salim et al. (2023) for the isophotal radius at 25 mag arcsec^{-2} in the r-band, given by their equation 6, which depends on stellar mass and the effective radius.

The relation provided by Salim et al. (2023) includes a scatter of 0.05 dex, which we incorporate as log-normal random scatter to our

sizes. Assuming the B and SDSS g bands are very similar for SFMS galaxies, we utilize the wavelength dependence of the effective radius with stellar mass for the SFMS from Kawinwanichakij et al. (2021) to convert the SDSS r band into the g band. We adopt the mean value reported by de los Reyes & Kennicutt (2019) to convert the isophote into a star-forming radius, i.e. $R_{25}/R_{SF} = 1.83$. This value is then used to transform our SDSS R_{25} into R_{SF} radii, incorporating a random scatter of 0.08 dex.

Having defined the star-forming region for each galaxy in our sample (Calette et al., in preparation), we re-estimated the H I gas mass within R_{SF} by assuming an exponential disc profile for the total gas mass (i.e. $M_{gas} = M_{H_2} + M_{HI}$). We assumed that at large distances, the gas profiles of galaxies follow the H I size-mass relation, defined as the radius at which the average H I surface density profile reaches a value of $\Sigma_{HI,1} = 1\,M_\odot\,pc^2$ (Broeils & Rhee 1997). We compute for each galaxy H I radii, R_{HI}, utilizing the H I size-mass relation from Wang et al. (2016) and by adding a random scatter of 0.06 dex. Furthermore, we assumed that at distances of R_{SF}, the H I profiles are well-characterized by a disc profile. The final step is to compute the scale-length radius of the H I disc by solving the following fundamental equation:

$$\Sigma_{HI,1} - \frac{M_{HI}}{2\pi R_{d,HI}^2} \exp\left(-\frac{R_{HI}}{R_{d,HI}}\right) = 0, \tag{B1}$$

where $R_{d,HI}$ is the scale-length radius, which is the unknown variable in the above equation. Having obtained the scale-length radius we can then obtain the H I mass at any radii, in particular at R_{SF}. Consequently, we define the following quantities for the analysis of the Calette et al. (in preparation) data: $\Sigma_{SFR} = 0.95 \times SFR/\pi R_{SF}^2$, $\Sigma_* = M_*/\pi R_{SF}^2$, $\Sigma_{gas} = M_{gas}/\pi R_{SF}^2$, and $\Sigma_{H_2} = M_{H_2}/\pi R_{SF}^2$. In these definitions, SFR, M_*, and M_{H_2} represent the global SFRs and stellar masses from the sample, while M_{gas} is the gas mass within the star formation radius. Notice that in all the analyses described below, we only include galaxies with detections in both HI and H_2 gas masses.

The left panel of Fig. B1 displays the Kennicutt–Schmidt (KS) law for our sample (blue filled squares) in comparison to the de los Reyes & Kennicutt (2019) sample (cyan filled squares). The distribution structure of our data closely mirrors that of de los Reyes & Kennicutt (2019), which is reassuring given the meticulous steps taken to obtain our data. By definition, the global KS law is expressed as

$$\Sigma_{gas} = \alpha_{KS} \Sigma_{SFR}^\eta. \tag{B2}$$

The best-fitting parameters obtained from our sample are $n = 1.28 \pm 0.01$ and $\log A_{KS} = -3.6 \pm 0.02$, with a dispersion of 0.31 dex. Combining information from both data sets, we derive the following parameters: $n = 1.4 \pm 0.01$ and $\log A_{KS} = -3.79 \pm 0.01$, with a dispersion of 0.32 dex. Overall, we observe a strong agreement between both data sets, affirming that our sample accurately captures the structure of the global KS law.

The right panel of Fig. B1 illustrates the inverted global KS law, expressed as

$$\Sigma_{gas} = \alpha_{KS} \Sigma_{SFR}^\eta. \tag{B3}$$

For our sample, we find $n = 0.44 \pm 0.02$ and $\log \alpha_{KS} = 2.09 \pm 0.04$, with a dispersion of 0.19 dex. For completeness, we performed fits on the combined data set, incorporating the data from de los Reyes & Kennicutt (2019). The resulting parameters are $n = 0.43 \pm 0.02$ and $\log \alpha_{KS} = 2.08 \pm 0.03$. Importantly, we observe strong consistency between these parameters and the ones obtained from the previous
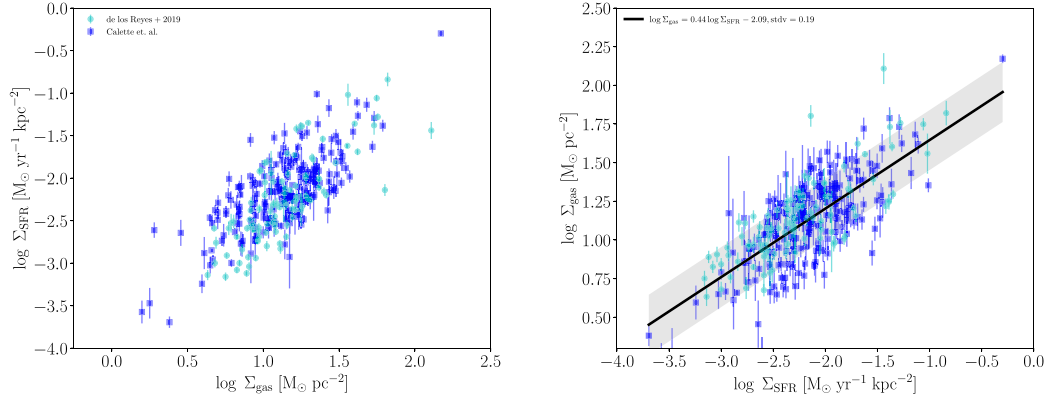
Figure B1. Left panel: Kennicutt–Schmidt law for our sample (see the text for details, blue filled squares) in comparison to the de los Reyes & Kennicutt (2019) sample (cyan filled squares). Overall, we observe a strong agreement between both data sets. Therefore, our sample accurately captures the structure of the global KS law. Right panel: Inverted global KS law. As described in the text, our main conclusions remain unbiased when including or excluding the data from de los Reyes & Kennicutt (2019) by fitting to a power-law model.
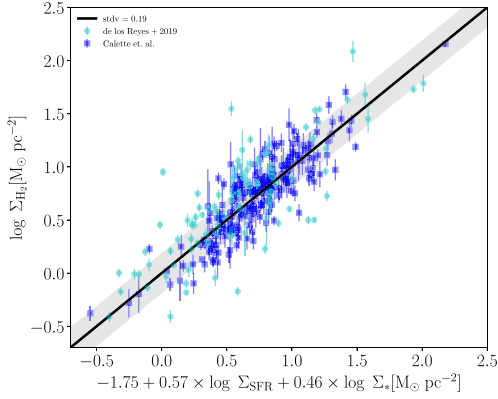
Figure B2. Best-fit model for our sample (blue filled squares), obtained by combining Σ_{SFR} and Σ_* to derive Σ_{H_2} as detail in the text. The predicted Σ_{H_2} values for the de los Reyes & Kennicutt (2019) sample is consistent with our best-fit model but exhibit a larger scatter.

fits. Therefore, whether including or excluding the data from de los Reyes & Kennicutt (2019), our main conclusions remain unbiased.

In Fig. B2, we present the best-fitting model for our sample (blue filled squares), obtained by combining Σ_{SFR} and Σ_* to derive Σ_{H_2}. The best-fitting model is expressed as

$$\Sigma_{H_2}(\mathrm{SFR}, M_*) = 10^{-1.75\pm0.03} \times \Sigma_{SFR}^{0.57\pm0.03} \times \Sigma_*^{0.46\pm0.05} \qquad \text{(B4)}$$

with a dispersion of 0.19 dex. Additionally, we compare the predicted Σ_{H_2} values for the de los Reyes & Kennicutt (2019) sample, which align with our best-fitting model but exhibit a larger scatter.

The predicted M_{gas} from our inverted global KS law versus the measured one, using the data from the Calette et al. (in preparation) compilation, is shown in the bottom panel of Fig. B3. The prediction nicely recovers the gas mass for the majority of the galaxies. Similarly, using the Calette et al. compilation, in the upper panel of the same figure we show that equation (B4) is a good predictor of the observed H_2 gas masses not only for star-forming galaxies but for quiescent ones.
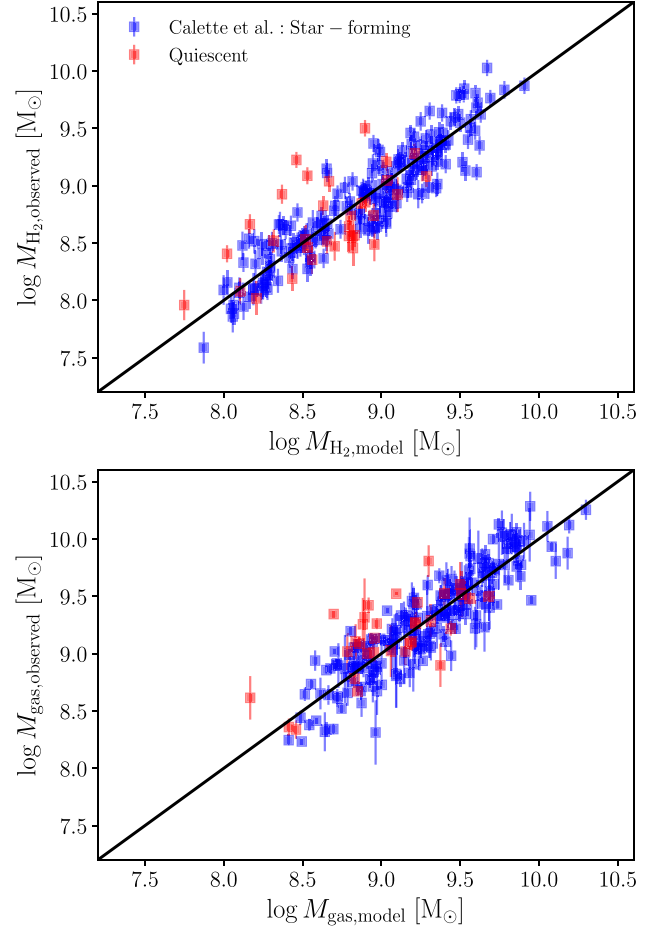
**Figure B3.** Comparison of the inferred H_2 (top panel) and total cold gas (bottom panel) masses with observations from the Calette et al. compilation (in preparation). Only H_2 and H I detections were considered. The solid red line represents the one-to-one relation.
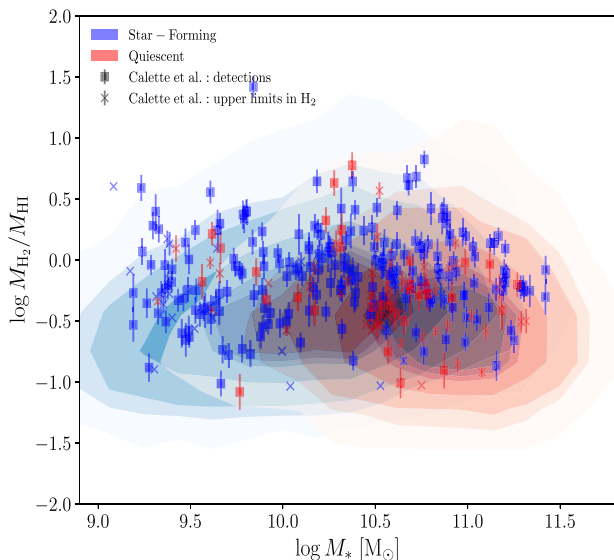
Figure B4. Predicted H_2/H I ratios as a function of M_* shown as blue and light red contours, respectively, for SFMS and quiescent (including GV) galaxies. The contours show 5, 16, 0.25, 5, 75, 84, and 95 per cent of the distribution. Blue (red) filled squares show the SFMS (quiescent) compilation from Calette et al. (in preparation, see also, Calette et al. 2018, 2021). The skeletal symbols show upper limits in H_2 but detections in H I. Notice how our model is consistent with the distribution of observed points.

Fig. 11 shows the H_2-to-H I mass ratio predicted by our model as a function of stellar mass for our SDSS galaxy sample. The sample of SFMS galaxies is shown by the blue-filled isocontours while GV and quiescent galaxies are shown in light red-filled isocontours. In the same panel, as a reference, we reproduce the Calette et al. compilation divided into star-forming an quiescent galaxies (filled squares represent detections in both H_2 and H I gas masses while crosses show non-detection in H_2) which is in good agreement with the distribution predicted by our model.
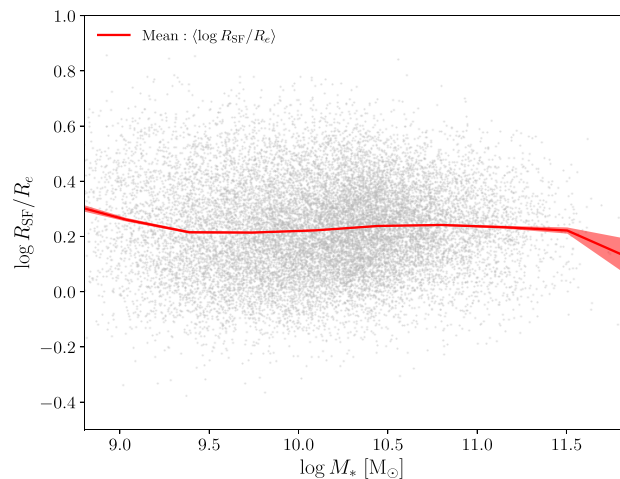
Figure B5. Ratio between the star-forming radius, R_{SF} and the half-light radius, R_e, as a function of stellar mass. The ratio depends little with mass but, on average, this is approximately $\langle \log R_{SF}/R_e \rangle \sim 0.23$.

Finally, in Fig. B5, we present the ratio between R_{SF} and R_e as a function of M_* for all our SDSS galaxies. The red line represents the mean $\langle \log R_{SF}/R_e \rangle$, and the shaded area indicates the error around the mean. It is noteworthy that this ratio exhibits little dependence on mass but is larger for low-mass galaxies and smaller for more massive ones. On average, this ratio is approximately $\langle \log R_{SF}/R_e \rangle \sim 0.23$.

This paper has been typeset from a T_EX/L^AT_EX file prepared by the author.